KTH Engineering Sciences

Quantification and Maximization of Performance Measures for Photon Counting Spectral Computed Tomography

MOA YVEBORG

Doctoral Thesis
Stockholm, Sweden 2015

TRITA-FYS 2015:08
ISSN 0280-316X
ISRN KTH/FYS/–15:08–SE
ISBN 978-91-7595-465-3

KTH FYSIK
SE-106 91 Stockholm
SWEDEN

Akademisk avhandling som med tillstånd av Kungl Tekniska högskolan framlägges till offentlig granskning för avläggande av teknologie doktorsexamen i fysik fredagen den 27 mars 2015 klockan 10.00 i D3, Lindstedtsvägen 5, Kungl Tekniska högskolan, Stockholm.

© Moa Yveborg, januari 2015

Tryck: Universitetsservice US AB, typsatt i LaTeX

Till Mattias och Liv.

Abstract

During my time as a PhD student at the Physics of Medical Imaging group at KTH, I have taken part in the work of developing a photon counting spectrally resolved silicon detector for clinical computed tomography. This work has largely motivated the direction of my research, and is the main reason for my focus on certain issues. Early in the work, a need to quantify and optimize the performance of a spectrally resolved detector was identified. A large part of my work have thus consisted of reviewing conventional methods used for performance quantification and optimization in computed tomography, and identifying which are best suited for the characterization of a spectrally resolved system. In addition, my work has included comparisons of conventional systems with the detector we are developing. The collected result after a little more than four years of work are four publications and three conference papers.

This compilation thesis consists of five introductory chapters and my four publications. The introductory chapters are not self-contained in the sense that the theory and results from all my published work are included. Rather, they are written with the purpose of being a context in which the papers should be read.

The first two chapters treat the general purpose of the introductory chapters, and the theory of computed tomography including the distinction between conventional, non-spectral, computed tomography, and different practical implementations of spectral computed tomography. The second chapter consists of a review of the conventional methods developed for quantification and optimization of image quality in terms of detectability and signal-to-noise ratio, part of which are included in my published work. In addition, the theory on which the method of material basis decomposition is based on is presented, together with a condensed version of the results from my work on the comparison of two systems with fundamentally different practical solutions for material quantification. In the fourth chapter, previously unpublished measurements on the photon counting spectrally resolved detector we are developing are presented, and compared to Monte Carlo simulations. In the fifth and final chapter, a summary of the appended publications is included.

Keywords: spectral computed tomography, silicon detector, detectability index, photon counting, Hotelling SDNR, material basis decomposition

Sammanfattning

Under min tid som doktorand på Medicinsk Bildfysik, KTH, har jag tagit del i arbetet med att utveckla en fotonräknande detektor med spektral upplösning för klinisk datortomografi. Detta arbete har till stor del motiverat inriktningen på min forskning, och de frågeställningar jag har valt att behandla. Tidigt i arbetet uppstod ett behov av att kvantifiera och optimera de egenskaper som karakteriserar en spektral detektor. Stor vikt har lagts på att revidera konventionella metoder för kvantifiering av prestanda med anpassning till spektrala system, samt hur ett sådant system ska jämföras med de detektorer som för närvarande används kliniskt. Det sammanställda resultatet av drygt fyra års arbete är fyra stycken publikationer samt tre konferensbidrag.

Denna avhandling består av en kappa och mina fyra publikationer. Kappan syftar till att sätta publikationerna i ett sammanhang, och är i sig inte självständig i den meningen att alla resultat från min forskning är inkluderade. Det två första avsnitten går kort igenom syftet med kappan, samt teorin bakom datortomografi och skillnaden mellan konventionell (dvs. icke energi-upplöst) datortomografi och olika tillämpningar av spektral datortomografi. Tredje avsnittet består av en revidering av konventionella metoder för kvantifiering och optimering av bildkvalitet i termer av detekterbarhet samt signal-brusförhållande. Utöver detta framförs teorin som ligger till grund för metoden materialbasdekomposition, vilken möjliggör för kvantifiering av material. I samband med detta presenteras en kort sammanfattning av resultaten från mitt arbete med att jämföra två olika system med spektral upplösning vars egenskaper i praktiken leder till fundamentalt olika tillvägagångssätt för att utföra materialbasdekomposition. I det fjärde avsnittet presenteras icke tidigare publicerade mätningar som utförts på den fotonräknande kiselbaserade detektorn som vår grupp har utvecklat, vilka även jämförs med Monte Carlo simuleringar. Det femte och sista kapitlet av kappan består av en sammanfattning av de fyra bifogade publikationerna.

Nyckelord: spektral datortomografi, kiseldetektor, detekterbarhet, fotonräknande, signal-brusförhållande, materialbasdekomposition

Publications

This thesis is based on the following papers:

I. M. Yveborg, M. Danielsson, H. Bornefalk. Performance evaluation of a submillimeter spectrally resolved CT system on high- and low-frequency imaging tasks: a simulation. *Phys. Med. Biol.*, 57:2373, 2012.

II. M. Yveborg, M. Persson, J. Crafoord, M. Danielsson and H. Bornefalk. Eliminated risk of iodine contrast cancellation with multibin spectral CT. *Phys. Med. Biol.*, 58:201-209, 2013.

III. M. Yveborg, M. Danielsson and H. Bornefalk. Theoretical comparison of a dual energy system and photon counting silicon detector used for material quantification in spectral CT. *IEEE Trans. Med. Imaging*, 34(3):796-806, 2014.

IV. M. Yveborg, M. Persson and H. Bornefalk. Optimal frequency-based weighting for spectral x-ray projection imaging. *IEEE Trans. Med. Imaging*, 34(3):779-787, 2014.

Reprints were made with permission from the publishers.

The author has contributed to the following publications, which are to some extent related to the thesis but not included.

- M. Yveborg, M. Danielsson and H. Bornefalk. Task based weights for spectral computed tomography. *Proc. of SPIE, Physics of Medical Imaging*, 831334-1–6, 2012.
- M. Yveborg, M. Danielsson and H. Bornefalk. Performance evaluation of a sub-millimeter spectrally resolved CT system on pediatric imaging tasks: a simulation. *Proc. of SPIE, Physics of Medical Imaging*, 7961:79615W-1-12, 2011.
- M. Yveborg, E. Fredenberg, C. Xu and M. Danielsson. Photon Counting CT with Silicon Detectors: Feasibility for Pediatric Imaging. *Proc. of SPIE, Physics of Medical Imaging*, 7258:725825-1–6, 2009.
- M. Persson, B. Huber, S. Karlsson, X. Liu, H. Chen, C. Xu, M. Yveborg, H. Bornefalk and M. Danielsson. Energy-resolved CT imaging with a photon-counting silicon-strip detector. *Phys. Med. Biol.*, 59:6709-6727, 2014.
- M. Persson, B. Huber, S. Karlsson, X. Liu, H. Chen, C. Xu, M. Yveborg, H. Bornefalk and M. Danielsson. Energy-resolved CT imaging with a photon-counting silicon-strip detector. *Proc. of SPIE, Physics of Medical Imaging*, 9033:90333L-1–10, 2014.
- C. Xu, M. Yveborg, H. Chen, M. Danielsson, S. Karlsson, C. Svensson and H. Bornefalk, Evaluation of an ultra-fast photon-counting energy-resolved ASIC for spectral CT. *Proc. of SPIE, Physics of Medical Imaging*, 8313:83130Y-1–6, 2012.

Contents

Publications **vii**

Contents **ix**

1 Purpose **1**

2 Introduction **3**
- 2.1 X-ray imaging 3
- 2.2 Computed Tomography 3
  - 2.2.1 CT system and parameters 4
  - 2.2.2 CT applications 4
  - 2.2.3 Dose 5
  - 2.2.4 CT detector technology 5
  - 2.2.5 Other imaging modalities 6
- 2.3 Interactions of photons with matter 6
  - 2.3.1 Rayleigh scattering 7
  - 2.3.2 Compton scattering 7
  - 2.3.3 The photoelectric effect 8
  - 2.3.4 Pair production 8
- 2.4 Limitations of current detector technology 8
- 2.5 Spectral computed tomography 11
  - 2.5.1 Quantification of performance of a spectrally resolved detector 12
  - 2.5.2 Outline 15

3 Quantification of detector performance **17**
- 3.1 Quantification of detectability 17
  - 3.1.1 Rose model 17
  - 3.1.2 Statistical decision theory 18
  - 3.1.3 Linear systems theory 20
  - 3.1.4 Choice of figure of merit for system comparison 25
- 3.2 Optimal energy weighting in spectral projection imaging 26
  - 3.2.1 Frequency-based weighting 27
- 3.3 Material basis decomposition 31

    - 3.3.1 Quantification of material basis decomposition accuracy . . . 33

4 Measurements of detector performance 39

- 4.1 MTF . . . 39
- 4.2 NPS . . . 40
- 4.3 DQE of photon counting silicon detector . . . 40
    - 4.3.1 MTF . . . 42
    - 4.3.2 NPS . . . 43
    - 4.3.3 DQE . . . 43
    - 4.3.4 Electronic noise . . . 45

5 Summary of the appended papers 49

- 5.1 Paper A: Performance evaluation of a sub-millimeter spectrally resolved CT system on high- and low-frequency imaging tasks: a simulation . . . 49
- 5.2 Paper B: Eliminated risk of iodine contrast cancellation with multibin spectral CT . . . 49
- 5.3 Paper C: Theoretical comparison of a dual energy system and photon counting silicon detector used for material quantification in spectral CT . . . 50
- 5.4 Paper D: Optimal frequency-based weighting for spectral X-ray projection imaging . . . 50
- 5.5 Contribution by co-authors . . . 51

Acknowledgements 53

Bibliography 103

Chapter 1

Purpose

This compilation thesis concerns the optimization and performance quantification of a spectrally resolved photon counting detector for computed tomography. It consists of five introductory chapters, followed by four appended papers based on simulations and theoretical modeling of X-ray imaging detectors. The introductory chapters are not self-contained in the sense that the theory and results from all my published work are included. Rather, they are written with the purpose of being a context in which the papers should be read. Hopefully, it supports the published work by providing some clarity to why I have chosen certain performance metrics and models when comparing and evaluating different systems.

For readers not familiar with the topic of computed tomography, the thesis starts with a chapter containing a short introduction to the subject of X-ray imaging and CT detector technology, followed by a chapter covering some different metrics of performance quantification and optimization. As an illustration to the topics of system comparison and optimization, a somewhat condensed account of parts of my published work is also included.

In theory there is no difference between theory and practice. In practice however, there is [1]. To emphasize the importance of comparing theoretical models with measurements, previously unpublished results from physical measurements on a spectrally resolved detector developed by the Physics of Medical Imaging group at KTH are presented in the final introductory chapter, and compared with simulations.

Chapter 2

Introduction

2.1 X-ray imaging

Working as a professor of physics at the university of Würzburg, Bavaria, in 1895, Wilhelm Röntgen was studying the phenomena accompanying the passage of an electric current through a tube filled with gas of extremely low pressure. Although he covered the tube in black paper and the room was completely dark, he noticed that a screen covered in fluorescent material placed as far as two meters from the tube was illuminated. By placing the hand of his wife in the path of the rays over a photographic plate, he observed after development of the plate an image displaying the bones of the hand. This image was the first “roentgenomgram” ever taken and Röntgen, not knowing the nature of these new rays, named them X-rays [2]. The discovery of X-rays, for which Röntgen in 1901 received the first Nobel prize in physics, truly came to revolutionize medicine. For the first time ever, the body's interior could be made visible without surgical intervention.

2.2 Computed Tomography

In 1917, Johann Radon provided the mathematical basis for computed tomography (CT) image construction by introducing the integral transform (now denoted Radon transform), demonstrating that the image of a 2-dimensional object can be reconstructed from an infinite number of 1-dimensional projections of that object [3]. The basic principle behind CT consists of acquiring a large number of X-ray projection images at different angles through the object under investigation. As compared to classical radiographs where only the relative distribution of the X-ray intensity is recorded, both the intensity attenuated by the object being examined and the primary, unattenuated intensity, are recorded. From these measurements, a computer can reconstruct digital format images which represent slices of the of the body's interior [4].

One of the most important feature of CT is the increased contrast as compared to radiographs. Contrast is defined as the difference in intensity between two neighboring elements [5]. In radiographs, the overlapping of many fine anatomical structures along the X-ray beam (denoted “anatomical noise”) is a major limiting factor, and cannot be overcome using this method [6]. With slice imaging, contrast is given by the difference in attenuation values of volume elements and not by values representing the attenuation through a line passing the whole object. Contrast is thus decided by the local composition and the problem of hidden structures is largely eliminated [5].

2.2.1 CT system and parameters

The first computed tomography system was built by Godfrey Hounsfield in 1971 [7]. It consisted of a pencil beam which was translated and rotated around the patient to generate an image. To speed up image acquisition time, detectors were eventually added allowing the use of a small fan beam. Despite this, scan times were several minutes long, causing artifacts and loss of image sharpness due to patient motion. In the 1980’s, continuously rotating CT system were introduced, based on the “slip ring technology” which dramatically reduced the amount of time needed for image acquisition, also providing the basis for fast volume scanning using spiral CT [5].

A modern clinical CT systems consists in short of a fan-beam geometry with an X-ray tube acting as source, and a detector. In a measurement, the source emits a beam which is attenuated by the object. The attenuated intensity is recorded by the detector from which an attenuation profile (projection) consisting of the natural logarithm of the ratio of the primary (unattenuated) and attenuated intensity is constructed. Next, the source and detector is moved and another projection is performed. Typically in modern CT systems, the rotation is performed continuously over 360 degrees providing slice image acquisition times of less than 1 second [7].

2.2.2 CT applications

CT is a widely used imaging method, both for patient diagnosis, treatment and follow-up. Two commonly reasons for using CT is to look for haeammorhages in the brain [8–11] or for detecting tumors, both in adult and pediatric CT. Another important application widely used is CT angiography (see e.g. [12]). In these examinations a contrast agent, commonly iodine, is injected into the patient. The high-attenuation contrast agent absorbs X-rays strongly and is used in order to provide detailed images of the blood vessels. Since coronary heart diseases is a major cause of death in today’s society [13, 14], it is of great interest to be able to early diagnose patients in the danger-zone of atherosclerois. One indication of coronary heart diseases is considered to be calcifications in the coronary arteries. With CT angiography, the possibility of displaying these calcifications and thereby evaluating the severity and extent of atherosclerosis, has been facilitated.

2.2.3 Dose

Computed tomography is considered to be a relatively high dose examination procedure. The major health risk known currently from the doses delivered in a CT scan is radiation-induced carcinogenesis. Only in the United States, it is estimated that 85 million CT scans are done every year (2011), where about 4 to 9 million of these are performed on children [15]. The number of CT scans has increased dramatically in only twenty year, from about 3 million (1981) (in the United states) to today's number. This increased use is mostly due to the development of CT as a fast and user-friendly examination.

The patient dose naturally depends on several parameters. Among these is not only the output from the X-ray tube (mAs, kVp, filtration) but also the patient size, volume being scanned and which part of the body that is being examined. Children are more sensitive to radiation-induced carcinogenesis and have, compared to adults, many remaining years left for cancer to develop. Since CT undoubtedly is an essential and powerful tool for imaging and diagnosis it is of high importance to continue the development of new CT techniques that have the capability of producing equal or higher image quality than today's system while delivering a lower dose, especially in pediatric CT. Several methods have been suggested to reduce the radiation dose associated with CT [16–18], for example using automatic exposure control or lowering the kVp [19].

2.2.4 CT detector technology

The detector records the attenuated radiation and constitutes one of the most important and technically complex part of the CT system. Its purpose is to transform the incident intensity to a signal. The most commonly used detector type in clinical CT systems is scintillator detectors [5, 20] which emit light in proportion to the amount of X-rays absorbed in the detector. The light is collected by a photodiode which converts it to an electrical current. Next, the electrical current is passed to an analog to digital converter which integrates the current from the photodiode over a certain sampling time [21]. A digital-to-analog converter (DAC) produces a digital number which represents the detected signal during the sampling time. Gadolinium oxysulfide (GOS) ceramic, ultra fast ceramic (UFC) and Gemstone are three common scintillator materials presently used in modern high-end, so called *energy integrating*, CT scanners [22–25]. In this type of detector, the energy information in terms of the energy dependent difference in linear attenuation coefficients, is lost as a result of the integration process. In addition, the electronic noise produced by readout electronics and detector sensors is also integrated into the signal.

The use of energy discriminating photon-counting detectors in clinical CT has been made feasible due to recent advances in detector technology and application specific integrated circuits (ASICs). In this type of detector, the X-ray photons interacting in the semiconductor sensors are converted to electron hole pairs without any intermediate process which ensures a superior intrinsic energy resolution [26, 27]. To retain a good energy resolution and process each pulse originating from photon conversion, an ultra fast photon-counting ASIC with energy discriminating capabilities is needed [28]. In practice, the energy-discrimination can be realized by the use of multiple energy thresholds which may also be used to reject electronic noise by setting the lowest threshold above the noise floor.

Two main types of materials have been proposed for photon-counting CT detectors: cadmium telluride/cadmium zink telluride (CdTe/CZT) [29–33] and silicon (Si) [34–36]. The major drawback using silicon is the relatively low atomic number compared to CdTe/CZT which makes it a worse photoelectric absorber. The result is a high fraction of Compton interactions, which in turn deteriorates its energy resolution as well as spatial resolution. CZT on the other hand, has been shown to suffer from pileup already at flux rates ten times lower than those encountered in clinical practice [37]. Silicon, compared to CZT, has short collection times of induced charge carriers and is thus less prone to intrinsic pile-up of signals at high detection rates [28].

2.2.5 Other imaging modalities

The most common alternatives to CT scans are ultrasound and Magnetic Resonance Imaging (MRI) (see e.g. [12, 38, 39]). Each method uses different principles to generate an image, and subsequently has its own areas where it is most effective. In ultrasound, high frequency sound waves are used for imaging, with the benefit of no radiation dose. However, ultrasounds are blocked by bone, thus limiting the cases where it can be used [40, 41]. In MRI, images are constructed based on measurements of how the hydrogen atom absorb and emit electromagnetic energy using powerful magnets [41].

An obvious advantage of both MRI and ultrasound compared to CT, is that the former do not involve exposing the patient to ionizing radiation. A major drawback with MRI is the time needed for image acquisition, often 45 minutes or more, making MRI less suitable for trauma patients. In addition, MRI cannot be used for patients with metal implants (e.g. pacemaker or metal clips in the head). Because of the long time needed for an MRI examination, children are often sedated to reduce artifacts from movement, which also is a risk factor. MRI is generally considered better at visualizing subtle differences between different kinds of soft tissues compared to CT, and CT to be better at providing details about bony structures [41].

2.3 Interactions of photons with matter

As photons traverse an object they can be scattered, absorbed or transmitted undisturbed [42]. For a certain material, photons with distinct energies will be attenuated differently. The linear attenuation coefficient (denoted μ with units of inverse length, cm^{-1}) is a measure of how photons interact with matter. It represents the exponential probability per unit path length in the absorber that an X-ray photon will be absorbed or scattered. In Fig. 2.1, examples of the attenuation coefficients of bone and soft tissue are shown as a function of photon energy E in the range of 1 to 80 keV [43].

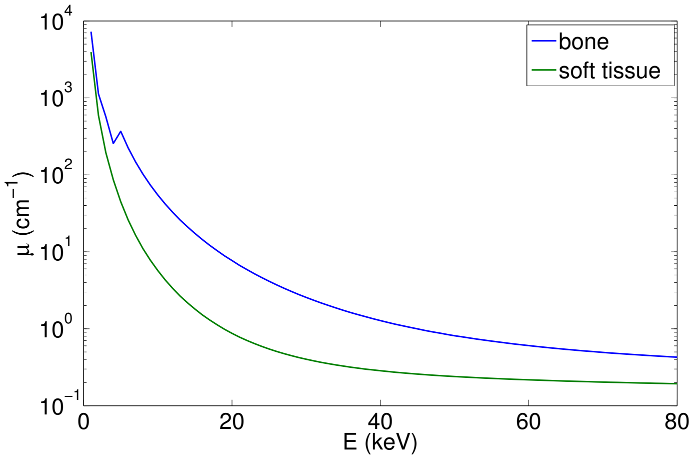

Figure 2.1: Figure showing the linear attenuation coefficient (μ) of soft tissue and bone as a function of photon energy E (keV).

The linear attenuation coefficient μ can be written as the sum of the individual linear attenuation coefficients for each photon interaction type, very briefly described below, according to [41]:

$$\mu = \mu_{\text{Compton scatter}} + \mu_{\text{photoelectric effect}} + \mu_{\text{Rayleigh scatter}} + \mu_{\text{pair production}}. \tag{2.1}$$

2.3.1 Rayleigh scattering

Rayleigh scattering occurs mainly with very low energy photons ranging from 15 to 30 keV. In this type of interaction, the incident photons cause the electrons in the scattering atom to oscillate in phase, whereby a photon is emitted with the same energy as the incident but in a slightly different direction. Since no electronics are ejected, no ionization of matter occur [41].

2.3.2 Compton scattering

Compton scattering is the dominating interaction of X-ray photons with soft tissue in the diagnostic imaging range, from 26 keV to approximately 30 MeV. In this event, an electron is ejected from the atom and the photon is scattered with a reduction in kinetic energy, resulting in an ionization of the absorbing matter. The angles of the scattered photon and electron depend on the energy of the incident photon. The probability of Compton scattering increases as the incident photon energy increases. The probability does not solely depend on the energy however, but also on electron density (number of electrons/g · density). Since the number of electrons/g is fairly constant in tissue, the probability of Compton scattering/unit volume can be approximated as to being proportional to the density of the object in X-ray imaging of tissue [41].

2.3.3 The photoelectric effect

When all of the incident photon energy is transferred to an electron and this electron is ejected from the atom, the process is called photoelectric absorption [41]. For this type of event, the energy of the incident photon must be greater than or equal to the binding energy of the electron. Since an electron is ejected, the absorbing matter is ionized. The probability of photoelectric absorption per unit mass is approximately proportional to Z^3/E^3, where E equals the energy of the incident photon and Z is the atomic number of the atom being ionized.

2.3.4 Pair production

Pair production only occurs when the energies of the X-rays exceed 1.02 Mev [41]. Since for a regular CT examination, the tube voltage normally does not exceed 140 keV, it is as such not a typically occurring event.

2.4 Limitations of current detector technology

A beam of mono-energetic photons with energy E and incident flux Φ_0 (photons per unit time and area) passing along a line l through a material with linear attenuation coefficient $\mu(x, y)$ will have an emerging photon flux Φ as given by an application of Lambert-Beer's law [42] :

$$\Phi = \Phi_0 \mathrm{e}^{-\int_l \mu(x,y)\mathrm{d}s}. \tag{2.2}$$

In CT, the projection value $p(t, \theta)$ at position t for a single view taken at angle θ for a parallel-beam geometry, is then defined as [44]

$$p(t, \theta) = \ln\left(\frac{\Phi}{\Phi_0}\right) = -\int_{l(t,\theta)} \mu(x, y)\mathrm{d}s. \tag{2.3}$$

In Eqs. (2.2) and (2.3), the integrals are along a line l that is at distance t from the origin and at angle θ off the x-axis as illustrated in Fig. 2.2. The value of t onto which the point (x, y) is projected with an angle θ, can be written as

$$t = x\cos(\theta) + y\sin(\theta). \tag{2.4}$$

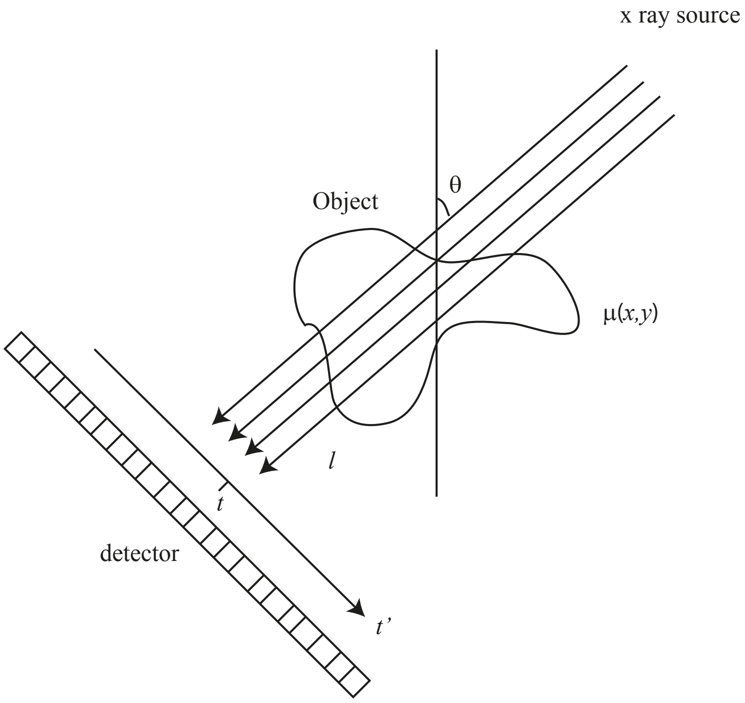

Figure 2.2: Figure illustrating a parallel-beam projection through an object.

Using Eq. (2.4), Eq. (2.3) can be formulated as

$$p(t,\theta) = \int_{-\infty}^{\infty} \int_{-\infty}^{\infty} \mu(x,y)\delta(x\cos(\theta) + y\sin(\theta) - t)\mathrm{d}x\mathrm{d}y. \tag{2.5}$$

The function above in Eq. (2.5), is the Radon transform. The projection slice theorem tells us that for an infinite number of projections, $\mu(x,y)$ can be perfectly reconstructed [45]. This is equal to finding the inverse Radon transform. In practice, most CT systems utilize a stabilized and discretized version of the inverse Radon transform, known as the filtered back projection algorithm, to reconstruct $\mu(x,y)$ [44].

For the case of mono-energetic photons as in the example above, a CT image would consist of cross-sectional map of the linear attenuation coefficient $\mu(x,y)$ at energy E of the patients anatomy. The X-ray beam emitted from the tubes used in computed tomography is however polychromatic, meaning that the photons are distributed over a range of energies which is illustrated in Fig. 2.3, showing a typical (normalized) CT spectrum of photons filtered with 5 mm of aluminum and a tube peak voltage of 80 kVp [46]. Conventional CT systems use a detector which rather than counting each photon separately, uses charge integrating methods where the signal is proportional to the amount of energy deposited in the detector. Detectors of this type are largely insensitive to the spectral information contained in the attenuated beam since it is not the linear attenuation coefficient at a certain energy that is measured, but rather an average taken over the spectrum being used [5]. Since the measured effective attenuation coefficient for such a system depends strongly on the spectrum shape, comparison between different values obtained from various systems is difficult. To mitigate this, a so called CT value in Hounsfield units (HU) has been defined (for compactness here denoted ξ) [5]:

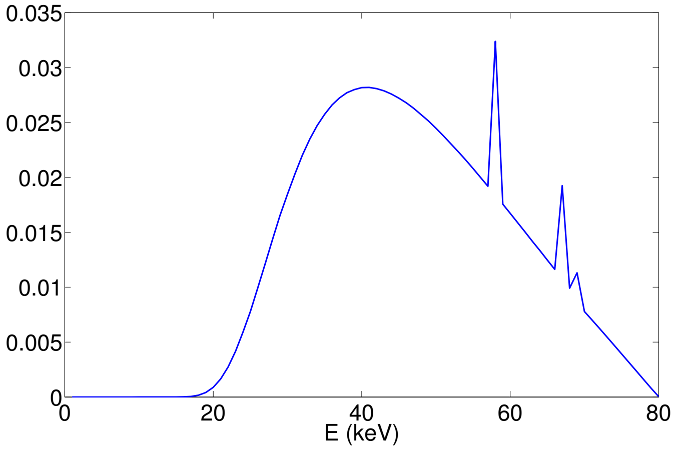

Figure 2.3: Figure shows a typical (normalized) photon spectrum used in CT. The tube peak voltage is 80 kVp and the spectrum is filtered with 5 mm of aluminum.

$$\xi = 1000\frac{\mu_t - \mu_w}{\mu_w}. \tag{2.6}$$

In Eq. (2.6), μ_t is equal to the reconstructed effective linear attenuation coefficient for the object being studied and μ_w the reconstructed effective linear attenuation coefficient of water.

In practice, the spectrum averaging means that two distinct materials such as calcified plaque and iodine-contrast-media-filled blood may result in the same range of attenuation values in a reconstructed CT image [7, 47]. This effect is illustrated in Fig. 2.4, showing a tomographic image of a PMMA phantom containing five columns of drilled holes of various sizes filled with iodine dissolved in water in concentrations of 1, 2, 4, 8 and 16 mg ml^{-1}, taken using clinical energy integrating CT (GE Lightspeed VCT, Milwaukee, USA) with a tube potential of 120 kV [47].

For the middle column containing 4 mg ml^{-1} of iodine, the contrast between the iodine solution and background material (PMMA) is zero. When increasing or decreasing the amount of iodine, i.e. the second and fourth columns containing 2 mg ml^{-1} and 8 mg ml^{-1}, respectively, the contrast increases and the iodine solution becomes visible.

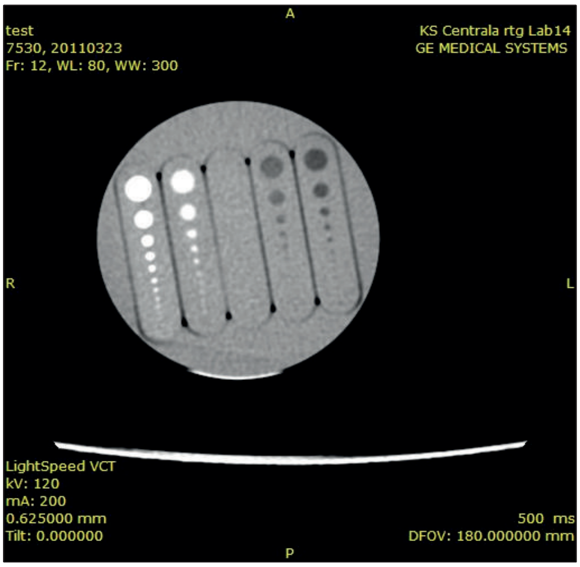

Figure 2.4: Tomographic image of a PMMA phantom containing drilled holes filled with iodine solution acquired using a clinical energy integrating detector at a tube potential of 120 kV. From right to left, the iodine concentrations are 1, 2, 4, 8 and 16 mg/ml. Note that full contrast cancellation occurs for 4 mg/ml.

Clinical examples of contrast cancellation include hypervascular hepatic tumors which can be hypodense to the surrounding liver prior to contrast enhancement but change into isodense or hyperdense lesions with increasing amount of iodine uptake [48]. Similarly a renal hemorrhage, normally hyperdense, might become hypodense once the kidney is filled with iodine. Common for these examples is the transition from a hypodense to hyperdense volume (or the reverse) following the uptake of contrast agent. At some point during this conversion, i.e. for some iodine concentrations, the effective linear attenuation coefficient of the enhancing region will equal the effective linear attenuation coefficient of the non-enhancing region.

2.5 Spectral computed tomography

By adding information on the energy dependent attenuation properties of the object, the problem with distinct tissues displaying similar CT values may be overcome. The spectral information can be used to determine the local area density of an objects constituent tissue equivalent materials, a method denoted *material basis decomposition*. In addition, the spectral resolution enables energy weighting methods [49, 50] different from the conventional integrating scheme which can be used to increase the detectability of a certain target structure.

The potential benefits of using X-ray spectral information in medical imaging was realized early [51, 52]. Today, various technical solutions whereby energy information can be extracted exist. One category is dual energy CT where there presently are three different approaches clinically and commercially available [53]; the dual source system [54] using two X-ray sources running at distinct voltages with two corresponding detectors, fast switching kVp systems [55,56] based on only one source and a tube voltage that follows a pulsed curve, and dual layer detector systems [57]. Dual energy CT has shown promising results in terms of material discrimination [54,58] and a range of of clinical applications exists. Some examples include bone removal from the carotid [59], reconstruction of virtual noncontrast-enhanced images (thus reducing patient dose with a factor of two in cases were such images are required), quantification of iodine enhancement in lesions of solid organs [60], identification of gout tophi [61] and differentiation of kidney stones [62]. In addition, image quality can be increased by optimizing contrast [63], or alternatively by generating mono-energetic images [64]. As the second and most technically advanced category of spectrally resolved detectors are photon counting systems capable of detecting the individual photons and measuring the corresponding energy, described in Sec. 2.2.4.

2.5.1 Quantification of performance of a spectrally resolved detector

When developing new digital detectors for CT, one important step is to compare the new technology with current state-of-the-art. In contrast to conventional energy integrating detectors, using photon counting spectrally resolved detectors electronic noise can be removed, beam hardening artifacts eliminated [51], materials be separated and quantified [65–67] and lesion detectability increased using proper weighting of the photons [49,50]. Not only the capability of measuring the energies of the detected photons may differ between distinct systems, but also properties such as detector element size which affects the systems ability to detect small lesions. Depending on detector material, charge sharing and scattering in the detector induce noise correlations and reduce spatial resolution by smearing of the point spread function. Currently, no figure of merit exists that can take all of the above mentioned properties into account. To differentiate two systems based on distinct technologies, certain features connected to the specific systems must be singled out and evaluated.

Figure of merit for image quality

For a spectrally resolved digital CT detector, three essential performance metrics that characterize the systems intrinsic capabilities can be defined:

- Spatial resolution
- Spectral resolution
- Contrast resolution

CT image quality can be described in a variety of terms such as noise, low-contrast spatial resolution and low-contrast detectability. Spatial resolution is typically defined as the measure of how closely lines can be resolved in an image, and depends not only on physical parameters such as focal spot size and detector element dimensions, but on choice of reconstruction algorithm [68]. The low-contrast resolution is defined as the smallest object that can be visualized given a certain dose and contrast to background intensity, typically measured using phantoms containing low-contrast objects of different sizes. The low-contrast detectability represents the ability of a CT scanner to distinguish between objects that have similar X-ray attenuation coefficients. Small objects are more difficult to detect than larger objects of the same contrast to background intensity. In analogy, objects of the same size will be easier to visualize the larger the contrast to background intensity. The low-contrast detectability thus depends on both the size of the object and its contrast to background intensity. In addition, the presence of noise highly influences the visibility of a given object. The noise in itself depends on a range of factors such as dose, slice thickness, tube voltage, detector material, energy spectrum and reconstruction algorithm. Low-contrast detectability is typically determined using measurements of phantoms in combination with human observers, or alternatively using computer analysis [69]. In its simplest form, it is quantified in terms of the signal-difference-to-noise ratio (SDNR).

From a systems spectral resolution emerges two main methods: energy weighting and material basis decomposition. The latter formula enables differentiation and characterization of different materials in an object. Energy weighting deals with optimal weighting of the detected photons where different methods have been proposed (projection, image and task-based) that show a significant image contrast enhancement compared to the energy-integrating method [49, 50] in terms of increase SDNR.

It might be considered more stringent to separate the spatial/contrast and spectral resolution when comparing two systems. Since the spectral information can be used to increase the contrast, i.e. detectability, of a certain lesion using optimal weighting of the detected photons, and as well for quantifying the local area density of a material, the two characteristics (i.e. spectral and contrast resolution) are however not entirely separable. As far as energy integrating detectors go, for a certain selection of settings (e.g. photon spectrum) and object, the contrast resolution in an image given a fixed range of Hounsfield values is set and can not be changed post-acquisition. For a multiple-bin photon counting detector however, contrast resolution depends on which weights are being used and can be altered at any time using the projection measurements [49] or reconstructed bin-images [50].

Performance evaluation

Traditionally, evaluation of the performance of a CT system has been made using physical phantoms in combination with software analysis and human observer studies [70, 71]. This method has several advantages, as it can take image artifacts such as beam hardening and ring artifacts into account. In addition, it relies on physical measurements where no assumptions of system linearity or shift-invariance have been made. Obviously, it has been and will continue to be, a powerful tool for the quantification and comparison of detector performance. The downside of this method however, is that it requires a mature system and depends strongly on the choice of reconstruction algorithm in combination with the phantom being used. In addition, it is time consuming. When developing new technologies for CT, it is at an early stage important to be able to evaluate the relative impact for example detector element size has on system performance.

In digital projection X-ray imaging (e.g. radiographs), system evaluation is routinely performed using a Fourier-based metrics [72–76] based on the assumption of linearity and shift-invariance, which can be used to optimize a system for a certain detection task. More specifically, common figures of merits are the detective quantum efficiency (DQE) and detectability index (d') that describe the propagation of the signal-to-noise ratio (SNR) and signal-difference-to-noise ratio (SNDR), respectively, in imaging systems [77] as a function of spatial frequency. In spite of CT systems being neither linear nor shift-invariant, assuming so and determining the frequency-based projection SNR and SDNR can be of use at an early development stage as they offer a method of system evaluation before complete physical measurements and three-dimensional reconstruction for practical reasons can be performed. (In absolute values however, the projection DQE and projection detectability index d' are misguiding for CT systems as they do not take into account the effect the three-dimensional reconstruction process has on signal and noise due to for example aliasing [78, 79].) Several studies investigating the relationship between theoretical descriptions of imaging performance using a Fourier-based approach and the performance of real human observers, both for CT and radiographs, have been published. Results indicate that the theoretical Fourier-based metrics of detectability using simple model observers indeed can predict the performance of human observers on a reasonable level [80, 81].

The physical performance of a system in terms of DQE and d' may relatively easily be simulated under certain idealized conditions, thereby offering a base-line from which comparisons can be made. The dependance of detectability on rudimentary parameters such as detector element size or detector material can be examined or compared to the performance of other systems. Since theory rarely coincides perfectly with reality, it is of course important to compare the simulations with physical measurements.

For energy integrating and photon counting detectors, the concept of DQE and its associated metrics have been well defined for projection imaging [52, 82] (and as well the effect of three-dimensional reconstruction for CT imaging [78, 79]). With the emerge of multiple-bin photon counting detectors, these definitions must be revisited and reviewed in conjunction with optimal methods of how to weigh different energy bins. Since material basis decomposition of an object containing a K-edge material is performed using two fundamentally different methods for dual energy imaging and multiple-bin photon counting systems, a considered approach must be taken when comparing the accuracies accompanying each technique.

It should be noted that there are other important parameters that determine the quality of an image or the performance of a CT system which are not addressed in this work. Amongst them is temporal resolution, somewhat simplified defined as the time needed for acquiring a single image [20]. This is an important characteristic in for example cardiac imaging where the object (i.e. heart) is moving during image acquisition, and also in CT fluoroscopy which requires near "real-time" images.

2.5.2 Outline

In the following Secs. 3.1.1, 3.1.2 and 3.1.2, well-established metrics to quantify and optimize the detectability of a target structure embedded in a background are presented in terms of SDNR and pixel-based weighting using statistical decision theory. In Sec. 3.1.3 follows an introduction to the linear systems theory which includes a derivation of the DQE and optimal weighting for spectral projection imaging using a multiple-bin detector originally presented in [83]. The theory of material basis decomposition is briefly reviewed in Sec. 3.3, as well as illustrations of the implementation using dual energy CT and multiple-bin detectors. An example of how a comparison between the accuracies in material basis decomposition using these two inherently different systems may be conducted is given in Sec. 3.3.1. In Sec. 4, physical measurements of detector performance in terms of projection DQE and modulation transfer function (MTF) using a photon counting silicon detector with eight energy bins developed by the Physics of Medical Imaging group at KTH are presented and compared with simulations.

Chapter 3

Quantification of detector performance

3.1 Quantification of detectability

Along with the rapid development of X-ray imaging devices over the past decades, the understanding of the fundamental processes that governs image quality have evolved in conjunction with well-defined metrics for comparison and evaluation of different technologies. Sec. 3.1.2 contains a short summary of the statistical decision theory used for system analysis in Sec. 3.2.1 and [83]: a more comprehensive treatment can be found in [84].

3.1.1 Rose model

The Rose model, named after its formulator Albert Rose, was employed in order to account for the quantized nature of X-rays. It describes the signal-difference-to-noise ratio (SDNR) for the detection of a uniform object in a uniform background [85–89]. If $\bar{q}_0$ and $\bar{q}_b$ is the mean number of quanta per unit area in the region of the uniform object and background, respectively, the Rose signal-difference (denoted ΔS) is equal to

$$\Delta S = A(\bar{q}_b - \bar{q}_0), \tag{3.1}$$

where A is the object area. The noise is defined as the standard deviation σ_b in the number of quanta in an equally large area of uniform background. For uncorrelated background quanta, the noise can be described by Poisson statistics and $\sigma_b = \sqrt{A\bar{q}_b}$, and

$$\mathrm{SDNR} = \frac{A(\bar{q}_b - \bar{q}_0)}{\sqrt{A\bar{q}_b}} = C(\sqrt{A\bar{q}_b}), \tag{3.2}$$

where $C = (\bar{q}_b - \bar{q}_0)/\bar{q}_b$ is the contrast. Rose formulated a very simple but efficient criterium, stating that if $\mathrm{SDNR} \geq 5$, the object is visible.

3.1.2 Statistical decision theory

Assume two hypothesis H_1 and H_0, representing the presence and absence of some feature (e.g. a tumor or bone), respectively. We collect in total Q observations $\hat{g}_i$ where $i = 1, ..., Q$, each an outcome of a random variable. Let:

$$\boldsymbol{g} = \left(\hat{g}_1, ...\hat{g}_Q\right)^T, \tag{3.3}$$

be a $1 \times Q$ column-vector containing all these observations, and

$$\bar{\boldsymbol{g}}^m = \langle \boldsymbol{g} | H_m \rangle \tag{3.4}$$

be the expectation value of $\boldsymbol{g}$ under hypothesis $m = 0, 1$. The ideal linear observer forms the discriminant function $T(\boldsymbol{g}) = \boldsymbol{w}^\dagger \boldsymbol{g}$, equal to the inner product between the column vector of weights $\boldsymbol{w} = \left(w_1, .., w_Q\right)^T$, and $\boldsymbol{g}$ where † refers to the complex conjugate transpose (equal to the transpose T when $\boldsymbol{g}$ and $\boldsymbol{w}$ are real). The (squared) SDNR of $T(\boldsymbol{g})$ is then equal to

$$\mathrm{SDNR}^2 = \frac{\left(\boldsymbol{w}^\dagger \Delta \bar{\boldsymbol{g}}\right)^2}{\boldsymbol{w}^\dagger \left(\boldsymbol{K}^0 + \boldsymbol{K}^1\right) \boldsymbol{w}}, \tag{3.5}$$

where $\Delta \bar{\boldsymbol{g}} = \bar{\boldsymbol{g}}^1 - \bar{\boldsymbol{g}}^0$ is the expected signal difference between the hypotheses. $\boldsymbol{K}^m$ in Eq. (3.5) is the $Q \times Q$ auto-covariance matrix of $\boldsymbol{g}$ under hypothesis $m = 0, 1$, with entries $K^m_{i,j}$ given by

$$K^m_{i,j} = \langle \left(\hat{g}_i - \bar{g}_i\right) \left(\hat{g}_j - \bar{g}_j\right)^\dagger | H_m \rangle. \tag{3.6}$$

It can be shown that the optimal weights $\boldsymbol{w}$ that maximize Eq. (3.5) are given by (see pages 850-852 in [84])

$$\boldsymbol{w} = \left(\boldsymbol{K}^0 + \boldsymbol{K}^1\right)^{-1} \Delta \bar{\boldsymbol{g}}. \tag{3.7}$$

Now, Eq. (3.5) with $\boldsymbol{w}$ given by Eq. (3.7), yields the (squared) Hotelling SDNR:

$$\mathrm{SDNR}^2 = \Delta \bar{\boldsymbol{g}}^\dagger \left(\boldsymbol{K}^0 + \boldsymbol{K}^1\right)^{-1} \Delta \bar{\boldsymbol{g}}, \tag{3.8}$$

which is the upper bound for Eq. (3.5).

Pixel-based weighting applied to multiple-bin photon counting detector

Conventional pixel-based weights (superscript pb) are calculated by designing the ideal linear (Hotelling) observer model to discriminate between the hypotheses H_0: pixel belonging to background, and hypothesis H_1: pixel belonging to target. Assume a spectrally resolved photon counting detector with N bins acquiring two-dimensional projection bin images $I_i(x, y)$, each of size $M_x \times M_y$ where $i = 1, ..., N$. $\Delta \bar{\boldsymbol{g}}^{\mathrm{pb}}$ is then of size $1 \times N$ and contains the difference in expectation value of the pixel value in the target, and the expectation value of the pixel value in the background. The optimal pixel-based weights $\boldsymbol{w}^{\mathrm{pb}}$ is of size $1 \times N$ and calculated as (using Eq. (3.7)):

$$\boldsymbol{w}^{\mathrm{pb}} = \left(\boldsymbol{K}^{0,\mathrm{pb}} + \boldsymbol{K}^{1,\mathrm{pb}}\right)^{-1} \Delta\bar{\boldsymbol{g}}^{\mathrm{pb}}. \tag{3.9}$$

In Eq. (3.9), the two-dimensional auto-covariance matrix $\boldsymbol{K}^{m,\mathrm{pb}}$ is of size $N \times N$. For uncorrelated bin counts, $\boldsymbol{K}^{m,\mathrm{pb}}$ is diagonal with entries equal to the variance of the counts in the corresponding bin and the (squared) Hotelling-SDNR defined in Eq. (3.8), calculated using $\boldsymbol{w}^{\mathrm{pb}}$, $\Delta\bar{\boldsymbol{g}}^{\mathrm{pb}}$ and $\boldsymbol{K}^{m,\mathrm{pb}}$, is maximized for a single pixel. Due to the Poisson nature of photon counting statistics, the variance is the expected value and the formulas for maximizing the SDNR of a target structure with linear attenuation $\mu_{\mathrm{t}}(E)$ over a background with linear attenuation $\mu_{\mathrm{bg}}(E)$, originally proposed by Tapiovaara and Wagner [90], follow immediately from Eq. (3.9):

$$w\left(E\right) = \frac{N_{\mathrm{bg}}(E) - N_{\mathrm{t}}(E)}{N_{\mathrm{bg}}(E) + N_{\mathrm{t}}(E)}. \tag{3.10}$$

In Eq. (3.10), N is the detected photons with energy E in the pixel belonging to the background (bg) and target (t).

For pulse height discriminating detectors capable of incrementing the counts in energy bin i if the detected energy E is between energy thresholds T_{i-1} and T_i, Cahn *et al.* [91] and later Giersch *et al.* [92] demonstrated the optimal weights for bin i with an average energy E_i to be

$$w\left(E_i\right) \propto \frac{1 - \mathrm{e}^{-(\mu_{\mathrm{t}}(E_i) - \mu_{\mathrm{bg}}(E_i))d_{\mathrm{t}}}}{1 + \mathrm{e}^{-(\mu_{\mathrm{t}}(E_i) - \mu_{\mathrm{bg}}(E_i))d_{\mathrm{t}}}}. \tag{3.11}$$

In Eq. (3.11), the Beer-Lambert law have been used assuming a thickness d_{t} for a target with linear attenuation coefficient μ_{t} embedded in a background with linear attenuation coefficient μ_{b}. Niederlöhner *et al.* [93] later refined the work of Cahn *et al.* and Giersch *et al.* by calculating the optimal weights taking into account uncorrelated scattered radiation, which follow by adding external noise to the diagonal entries of $\boldsymbol{K}^{m,\mathrm{pb}}$ in Eq. (3.9):

$$w\left(E_i\right) \propto \frac{1 - \mathrm{e}^{-(\mu_{\mathrm{t}}(E_i) - \mu_{\mathrm{bg}}(E_i))d_{\mathrm{t}}}}{1 + \mathrm{e}^{-(\mu_{\mathrm{t}}(E_i) - \mu_{\mathrm{bg}}(E_i))d_{\mathrm{t}}} + 2 \times \mathrm{SPR}_i}, \tag{3.12}$$

where SPR_i is the scatter to primary ratio of bin i.

When constructing a weighted projection image $I\left(x, y\right)$, identical weights are used for all counts registered in bin i regardless of pixel location:

$$I\left(x, y\right) = \sum_{i}^{N} w_i^{\mathrm{pb}} I_i\left(x, y\right), \tag{3.13}$$

where w_i^{pb} refers to the ith entry in $\boldsymbol{w}^{\mathrm{pb}}$. Studies have shown that compared to energy integrating systems at the same patient dose, ideal photon-counting energy-sensitive detectors applying optimal energy weighting schemes have the potential to increase the contrast-to-noise ratio in CT images by 15-60% [49, 50].

3.1.3 Linear systems theory

The SDNR is important as it establishes that image quality ultimately is limited by the statistical nature of quanta. It is however in its simplicity an insufficient measure since it only is relevant in the limit where the structures to be detected in the image are uniform over very large areas. For smaller structures, the detector element (del) size limits the systems maximum achievable spatial resolution and one has to take the spatial frequency dependence of signal and noise into account.

Assuming a linear, shift-invariant and wide-sense stationary system, a Fourier-transfer linear-systems approach [94] is a more suitable measure to analyze or characterize system performance. It is used to describe both signal and noise transfer via the modulation transfer function (MTF) and noise power spectrum (NPS). Two associated metrics commonly used to quantify the performance of a digital detector in terms of detector effectiveness and detectability, are the detective quantum efficiency (DQE) and detectability index d'.

Listing all the contributors to the unified framework for system evaluation is not in the scope of this work but interested readers are referred to the work of Cunningham and Shaw [95] for a historical exposition and general overview, as well as to the introduction by Sattarivan and Cunningham [96] on how to estimate the DQE via the MTF and NPS by cascading elementary processes.

MTF

The point-spread function $\mathrm{psf}(x, y)$ is the response of a linear and shift-invariant system to an impulse located at $x = 0, y = 0$. The optical transfer function (OTF) is defined as the zero-frequency normalized Fourier transform of the point-spread function:

$$\mathrm{OTF}(u, v) = \frac{\mathcal{F}\{\mathrm{psf}(x, y)\}}{\mathcal{F}\{\mathrm{psf}(0, 0)\}}, \tag{3.14}$$

and $\mathrm{MTF}(u, v) = |\mathrm{OTF}(u, v)|$ where by definition, MTF is equal to 1 at zero spatial frequency coordinates u and v [72]. For an ideal system, the point-spread function is a delta function and the MTF flat and equal to unity for all frequencies. In practice, in addition to e.g. scattering of secondary quanta in the detector, the discrete sampling and integration of quanta in each detector element employed using digital detectors significantly alters the shape of the MTF.

For a digital detector with pixels of size a_x and a_y in the x- and y-direction, respectively, the integration of quanta can be modeled as a convolution with a rectangle function $\Pi(-x/a_x, -y/a_y)$ in the spatial domain. In the spatial-frequency domain, convolution translates into multiplication. The pre-sampling MTF is the

MTF of a digital system before the process of discrete sampling introduced by the sampling aperture and can be written as a product of the MTF from the point spread function and an aperture MTF (here denoted MTF_{a_x,a_y}) equal to:

$$\mathrm{MTF}_{a_x,a_y}(u,v) = \frac{|T_{a_x,a_y}(u,v)|}{T_{a_x,a_y}(0,0)} = |\mathrm{sinc}(\pi a_x u)||\mathrm{sinc}(\pi a_y v)|, \tag{3.15}$$

where $T_{a_x,a_y}(u,v) = \mathcal{F}\{\Pi(-x/a_x, -y/a_y)\}$.

For digital detectors, the discrete sampling at the centre of each detector element located at $(n_x x_0, n_y y_0)$ for all integers (n_x, n_y) introduces aliasing which can be modeled by multiplication with a comb function $\sum_{-\infty}^{\infty} \delta(x - n_x x_0, y - n_y y_0)$ in the spatial domain. In the spatial frequency domain, this corresponds to convolution with $(1/(x_0 y_0)) \sum_{n_y=-\infty}^{\infty} \sum_{n_x=-\infty}^{\infty} \delta(u-(1/n_x x_0), v-(1/n_y y_0))$. The sampling at uniform spacings of x_0 and y_0 in the x- and y-direction, respectively, thus corresponds to the production of aliases of the signal at spacings of $u = 1/x_0$ and $v = 1/y_0$ [72]. If these aliases overlap, i.e. the signal contains frequencies higher than $u = 1/(2x_0)$ and $v = 1/(2y_0)$, the image signal will be distorted at frequencies below the cut-off frequencies $u_{c,x} = 1/(2x_0)$ and $v_{c,y} = 1/(2y_0)$ according to the Nyquist-Shannon sampling theorem (see e.g. [97]).

From a 2-dimensional MTF, the 1-dimensional MTF can be estimated by

$$\mathrm{MTF}(u) = \mathrm{MTF}(u,v)|_{v=0}, \tag{3.16}$$

which is equal to evaluating $\mathrm{MTF}(u,v)$ along the $v = 0$ axis [72].

NPS

The autocovariance describes the correlation of a random variable $a(x)$:

$$\boldsymbol{K}_a(x', x'+x) = \mathbb{E}\{\Delta a(x') \Delta a^*(x'+x)\}. \tag{3.17}$$

It describes the correlation of $a(x')$ with itself at a location displaced by x. For a wide-sense stationary random process, the autocovariance in Eq. (3.17) depends on the separation x and not on the position x' [98], i.e. $\boldsymbol{K}_a(x', x'+x) = \boldsymbol{K}_a(x)$. The 1-dimensional NPS of a wide sense stationary process is equal to the Fourier transform of the 1-dimensional autocovariance matrix $\boldsymbol{K}$:

$$\mathrm{NPS}(u) = \mathcal{F}\{\boldsymbol{K}_a(x)\}. \tag{3.18}$$

The autocovariance in Eq. (3.17) is based on true expectation values which in practice may be difficult to obtain. For an ergodic process however, the expected values can be determined either by the spatial or ensemble average. The autocovariance can thus be estimated by the sample autocovariance $\boldsymbol{K}_{a,X}(x)$:

$$\boldsymbol{K}_{a,X}(x) = \frac{1}{X} \int_X \Delta a(x') \Delta a(x'+x) \mathrm{d}x', \tag{3.19}$$

which in the limit of $X \to \infty$, gives the autocovariance. Using Eqs. (3.18) and (3.19), the NPS of a wide-sense stationary ergodic random process can be written as

$$\mathrm{NPS}_a(u) = \lim_{X\to\infty} \frac{1}{X}\mathbb{E}\left\{\left|\mathcal{F}_X\left\{\Delta a(x)\right\}\right|^2\right\} \tag{3.20}$$

where $\Delta a(x)$ is a zero-mean noise-only function. For a 2-dimensional wide-sense stationary ergodic random process $d(x, y)$, the 2-dimensional NPS is given by

$$\mathrm{NPS}_d(u, v) = \lim_{X,Y\to\infty,\infty} \frac{1}{XY}\mathbb{E}\left\{\left|\mathcal{F}_{X,Y}\left\{\Delta d(x, y)\right\}\right|^2\right\}, \tag{3.21}$$

where $\Delta d(x, y)$ is a zero-mean noise-only function and $\mathcal{F}_{X,Y}\left\{\Delta d(x, y)\right\}$ is the 2-dimensional Fourier transform of $\Delta d(x, y)$.

In practice, the 1-dimensional NPS can be estimated from 1-dimensional digital data d_n of size $1 \times N$ according to [72]:

$$\mathrm{NPS}_{dig}(u) = \frac{x_0}{N}\mathbb{E}\left\{\left|\mathrm{DFT}\left\{\Delta d_n\right\}\right|^2\right\}. \tag{3.22}$$

In Eq. (3.22), $\Delta d_n = d_n - \mathbb{E}\{d_n\}$, x_0 the sampling distance and DFT equal to the discrete Fourier transform. For a 2-dimensional digital data d_{n_x,n_y} of size $N_x \times N_y$ with sampling distances x_0 and y_0 in the x- and y-direction, respectively, the 2-dimensional NPS is given by [72]

$$\mathrm{NPS}_{dig}(u, v) = \frac{x_0 y_0}{N_x N_y}\mathbb{E}\left\{\left|\mathrm{DFT}^{2D}\left\{\Delta d_{n_x,n_y}\right\}\right|^2\right\}, \tag{3.23}$$

where DFT^{2D} is the 2-dimensional discrete Fourier transform and $\Delta d_{n_x,n_y} = d_{n_x,n_y} - \mathbb{E}\{d_{n_x,n_y}\}$. From a 2-dimensional NPS, the one-dimensional NPS can be calculated as:

$$\mathrm{NPS}(u) = \mathrm{NPS}(u, v)|_{v=0}, \tag{3.24}$$

which is equal to evaluating the 2-dimensional NPS along the $v = 0$ axis.

Detective quantum efficiency and detectability index

The two-dimensional DQE for an average input number of quanta q per unit area is defined as [72]

$$\mathrm{DQE}\left(u, v\right) = \frac{\mathrm{NEQ}\left(u, v\right)}{q}, \tag{3.25}$$

where the $\mathrm{NEQ}\left(u, v\right)$ is defined as the square of the expected output signal S (at spatial frequency coordinates (u, v)) for a constant input signal q divided by the corresponding output NPS:

$$\mathrm{NEQ}\left(u, v\right) = \frac{|S(u, v)|^2}{\mathrm{NPS}\left(u, v\right)}. \tag{3.26}$$

The frequency dependent SDNR, commonly denoted detectability index d', is equal to the integral of the squared Fourier-based ideal observer SDNR:

$$d'^2 = \int \mathrm{SDNR}^2 \left(u, v\right) \mathrm{d}u \mathrm{d}v. \tag{3.27}$$

For a constant input number of quanta q per unit area, it is well known how the expressions in Eqs. (3.25), (3.26) and (3.27) translate for a single-bin (subscript sb) photon counting detector [72]. By writing the absolute value of the output signal $S\left(u, v\right)$ in the spatial frequency domain equal to the absolute value of the product of the average incoming signal q times the system OTF:

$$|S\left(u, v\right)| = q|\mathrm{OTF}\left(u, v\right)|, \tag{3.28}$$

we have:

$$\mathrm{DQE}_{\mathrm{sb}}\left(u, v\right) = \frac{qG^2 \mathrm{MTF}\left(u, v\right)^2}{\mathrm{NPS}\left(u, v\right)}, \tag{3.29}$$

$$\mathrm{NEQ}_{\mathrm{sb}}\left(u, v\right) = \frac{q^2 G^2 \mathrm{MTF}\left(u, v\right)^2}{\mathrm{NPS}\left(u, v\right)}, \tag{3.30}$$

and

$${d'_{\mathrm{sb}}}^2 = \Delta N^2 \int_{-\infty}^{\infty} \frac{h\left(u, v\right)^2 \mathrm{MTF}\left(u, v\right)^2}{\mathrm{NPS}\left(u, v\right)} \mathrm{d}u \mathrm{d}v. \tag{3.31}$$

In Eq. (3.31), we have assumed $h\left(u, v\right)$, equal to the Fourier transform of the object profile, to be strictly positive and normalized to 1 at frequency coordinates $(0, 0)$. ΔN is the total detected signal difference between the target and background. $G = d/q$ in Eq. (3.29), is the system large-area gain factor, where d is the average output signal.

For a multiple-bin system (subscript mb) with bins $i = 1, ..., N$ and input bin signal $d_i\left(x, y\right)$, the output bin signal $s_i\left(x, y\right)$ is given by $d_i\left(x, y\right) * \mathrm{psf}_i\left(x, y\right)$ where $\mathrm{psf}_i\left(x, y\right)$ is the point spread function for bin i and $*$ the convolution operator. Using a $1 \times N$ vector of bin weights $\boldsymbol{w}$ with entries w_i, the Fourier transform of the output signal is equal to the weighted sum of the Fourier transform of the bin input signals times the optical transfer function for bin i, $\mathrm{OTF}_i\left(u, v\right)$:

$$S\left(u, v\right) = \mathcal{F}\{s\left(x, y\right)\} = \sum_i^N w_i D_i\left(u, v\right) \mathrm{OTF}_i\left(u, v\right). \tag{3.32}$$

In Eq. (3.32), $D_i\left(u, v\right)$ is the Fourier transform of the input bin signal $d_i\left(x, y\right)$.

Because of the summation over bin signals, the absolute value of the output signal cannot be written as a product of the absolute value of the input signal and a system MTF. This implies that the NEQ, DQE and d' for a mean number of registered counts N_i in bin i per unit area, and mean number of input counts q_i in bin i per unit area, must be written in less concise forms compared to Eqs. (3.29), (3.30) and (3.31) [83]:

$$\mathrm{NEQ}_{\mathrm{mb}}\left(u,v\right) = \frac{\left|\sum_{i} w_{i} N_i \mathrm{OTF}_i\left(u,v\right)\right|^2}{\mathrm{NPS}\left(u,v\right)}, \tag{3.33}$$

and

$$\mathrm{DQE}_{\mathrm{mb}}\left(u,v\right) = \frac{\left|\sum_{i} w_{i} N_{i} \mathrm{OTF}_{i}\left(u,v\right)\right|^2}{\mathrm{NPS}\left(u,v\right)\sum_i q_i}. \tag{3.34}$$

Since the individual bin input counts q_i can be equal to zero, a bin-DQE cannot be defined; such a normalization would produce infinitely large quotients. Assuming a target consisting of a single material, the bin output signal $\Delta S_i\left(u,v\right)$ is equal to the total signal difference in bin i, ΔN_i, times $h\left(u,v\right)$, the Fourier transform of the object profile and the bin-OTF. The squared detectability index is then equal to:

$${d'_{\mathrm{mb}}}^2 = \int \frac{\left|\sum_i w_i \Delta N_i h\left(u,v\right)\mathrm{OTF}_i\left(u,v\right)\right|^2}{\mathrm{NPS}\left(u,v\right)} \mathrm{d}u\mathrm{d}v. \tag{3.35}$$

3D reconstruction

The three-dimensional NPS and MTF of the reconstructed image can be modeled according to the method outlined by Tward and Siewerdsen [79]. This method starts with normalization of the projection NPS according to $\mathrm{NPS}_{\mathrm{out}} = \mathrm{NPS}_{\mathrm{in}}/\bar{q}^2$, where $\bar{q}$ is the mean detector signal. The normalization is followed by an application of a ramp and an apodization filter whereby the NPS and MTF are transferred as a deterministic convolution, i.e. $\mathrm{NPS}_{\mathrm{out}} = \mathrm{NPS}_{\mathrm{in}}T^2$ and $\mathrm{MTF}_{\mathrm{out}} = \mathrm{MTF}_{\mathrm{in}}T$ at each stage (with T being the filter expressed in the Fourier domain). Any interpolation of the filtered projection is also transferred as a deterministic convolution. For a bilinear interpolation, T is given by $T = \mathrm{sinc}^2(\pi u a_u)\mathrm{sinc}^2(\pi v a_v)$ where a_u and a_v are the sampling distances in the projection image.

The 3D reconstruction stage affects the NPS as

$$\mathrm{NPS}_{\mathrm{out}}(f,w') = \frac{\pi}{mf}\mathrm{NPS}_{\mathrm{in}}(u/M, v/M), \tag{3.36}$$

where $f = (u^2 + v^{2)}$ is the radial spatial frequency in an axial slice in the reconstructed domain (u, v and w are the spatial frequency coordinates in the reconstructed 3D image). w' is the spatial frequency along the axis of rotation, M is the magnification and m the number of projections.

Using voxel-driven reconstruction, the effect of the 3D reconstruction process on the MTF is given by

$$\mathrm{MTF}_{\mathrm{out}}(f,w') = \frac{1}{Mf}\mathrm{MTF}_{\mathrm{in}}(u/M, v/M). \tag{3.37}$$

As a final step, the NPS 3D voxel matrix is again sampled introducing aliasing in three dimensions.

3.1.4 Choice of figure of merit for system comparison

The SNR is calculated as the ratio of the mean signal value S_B, to the standard deviation σ_{S_B} of the signal values over a given neighborhood:

$$\mathrm{SNR} = \frac{S_B}{\sigma_{S_B}}. \tag{3.38}$$

The SDNR is defined as the ratio of the mean signal-difference $S_B - S_A$, and the standard deviation σ_{S_B} of the background:

$$\mathrm{SDNR} = \frac{S_B - S_A}{\sigma_{S_B}}. \tag{3.39}$$

The contrast C is equal to the ratio of the mean signal-difference $S_B - S_A$, and the mean background signal S_B according to

$$\mathrm{C} = \frac{S_B - S_A}{S_B}. \tag{3.40}$$

Assume a detector which generates a signal proportional to the number of absorbed photons where the only noise source is due to the Poisson statistics of the absorbed photons. Then, $\sigma_{S_B} = \sqrt{S_B}$, which gives

$$\mathrm{SNR} = \frac{S_B}{\sigma_{S_B}} = \frac{S_B}{\sqrt{S_B}} = \sqrt{S_B}, \tag{3.41}$$

and

$$\mathrm{SDNR} = \frac{S_B - S_A}{\sigma_{S_B}} = \frac{S_B - S_A}{\sqrt{S_B}}. \tag{3.42}$$

The NEQ is equal to the square of the (spatial frequency-dependent) SNR:

$$\mathrm{NEQ} = \mathrm{SNR}^2 = S_B, \tag{3.43}$$

using Eq. (3.41). The DQE is defined as the NEQ divided by the mean input signal $S_{B,in}$:

$$\mathrm{DQE} = \frac{\mathrm{NEQ}}{S_{B,in}}. \tag{3.44}$$

For a system with unity detection efficiency and an NEQ as expressed in Eq. (3.43), $S_B = S_{B,in}$ and the DQE is equal to

$$\mathrm{DQE} = \frac{S_B}{S_{B,in}} = 1. \tag{3.45}$$

The detectability index is equal to the integral of the squared signal-difference-to-noise ratio:

$$\mathrm{SDNR}^2 = \frac{(S_B - S_A)^2}{S_B} = \mathrm{C}^2\mathrm{NEQ}. \tag{3.46}$$

Since the NEQ is a measure of the squared signal-to-noise ratio according to Eq. (3.33), it tells us nothing about the contrast detectability which is an important parameter when comparing different CT systems. Rather, the NEQ is measure of the *intensity* of the signal produced by the detector, and the DQE of the effectiveness of the detector. A certain CT system may be associated with a high NEQ and DQE but still produce images with very low contrast. Since for an energy integrating system, the contrast can cancel out for two materials with an on average equal attenuation, the detectability defined in Eq. (3.46) might even be zero (i.e. $S_B = S_A$). For the evaluation of a spectrally resolved system, this becomes especially important since the optimal energy weights defined in Eq. (3.7), are designed to maximize a signal-difference-to-noise ratio and as such are task dependent. Rather than being parameters of image quality, the NEQ and DQE should be used for evaluating the impact different physical parameters have on the spatial resolution of a specific system, such as detector material or size or detector element. When comparing two different systems, the detectability index d' is a more appropriate chose of figure of merit since it incorporates both the contrast and the NEQ, schematically according to Eq. (3.46) [52].

3.2 Optimal energy weighting in spectral projection imaging

For a multiple-bin photon counting detector, the still universal concept [49, 50, 99] of pixel-based bin-weights described in Sec. 3.1.2 cannot take into account spatial correlation structures between detector elements in different bin images and any difference in point spread functions of separate bins originating from photons depositing energy in several detector elements via Compton scattering and/or charge sharing. The same weighting scheme will therefore be used for the combination of imaging task and system giving rise to a large fraction of high spatial frequency dependent SDNR as for one with predominantly low spatial frequency dependent SDNR. This is can be illustrated by considering the pre-sampling projection MTF of each bin for a simulated multiple-bin photon counting silicon detector with five equidistantly placed energy thresholds and a pixel size of 0.5 mm, shown in Fig. 3.1. The amplitude of the MTF of bin number two (denoted MTF_2) at frequencies distinct from zero is considerably lower than the amplitudes of the other bin-MTFs. This is due to a large part of the Compton scattered photons depositing their energies in bin two, thereby smearing the point spread function of that bin. A pixel-based weighting scheme will only “see” the zero-frequency part of the bin-MTFs, thereby ignoring the amplitudes at higher frequencies even though they effect the DQE and detectability index according to Eqs. (3.34) and (3.35).

Bornefalk [100] pointed out this predicament and attempted to rectify it by developing a framework for maximizing the frequency-based detectability index d' for photon counting spectral projection images using task-based weights. Those weights were derived by taking the spatial frequency dependence of noise and signal

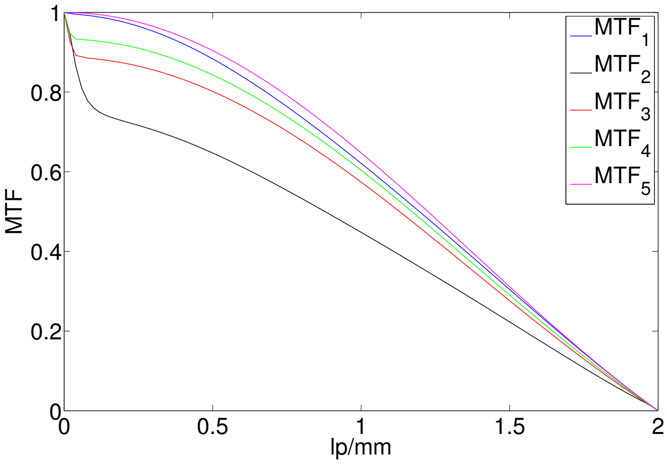

Figure 3.1: Bin-MTFs, denoted MTF_i where $i = 1, ..., 5$, for a simulated multiple-bin photon counting silicon detector with five equidistantly placed energy bins and a pixel size of 0.5 mm.

for each bin into account, and the final image $I(x, y)$ calculated as the weighted sum of the bin images $I_i(x, y)$:

$$I(x, y) = \sum_{i}^{N} w_i I_i(x, y), \tag{3.47}$$

where N are the number of bins. Since a small object contains both high and low frequencies, it may not however always be optimal to weigh all frequency components of a signal in a certain bin equally. For example, the frequency dependent SDNR in a particular bin may diminish for a certain range of frequencies due to a high degree of charge sharing, but remain high for others. Nevertheless, the weighting scheme used in Eq. (3.47) weighs all frequency components of the signal in that bin identically.

The idea of optimizing signal detectability by analyzing the frequency content of a certain imaging task is not new; prior to [100], Siewerdsen and Antonuk [101] optimized the CsI:Tl scintillator thickness for a chest radiography system. Further, Richard and Siewerdsen [102] and Fredenberg *et al.* [103] optimized the dose allocation and relative weights of high- and low-energy images in a dual energy application; other examples exist [104, 105].

3.2.1 Frequency-based weighting

Assume a spectrally resolved photon counting detector with N bins acquiring two-dimensional projection bin images $I_i(x, y)$, each of size $M_x \times M_y$ where $i = 1, ..., N$.

A different approach of calculating the weights defined in Eq. (3.7) originally presented in [83], is to find the linear discriminant that takes into account the information from all pixels, thus making $\bar{\boldsymbol{g}}^m$ and the covariance matrix K_m defined in Eqs. (3.4) and (3.6) of sizes $1 \times NM_xM_y$ and $(NM_xM_y) \times (NM_xM_y)$, respectively, for our hypothetical system. In the Fourier domain, this translates into taking every frequency component of - let's say- each bin-MTF in Fig. 3.1 into account in contrast to solely the zero-frequency value as for pixel-based weighting. We denote this type of weighting scheme *frequency-based* weighting, and show below that it provides the upper limit on the frequency-based SDNR for spectral projection imaging.

Theoretical framework

By writing the inverse discrete Fourier transform as a matrix multiplication [106], we have

$$\Delta\bar{\boldsymbol{g}} = \boldsymbol{H}^{-1}\Delta\tilde{\bar{\boldsymbol{g}}}, \tag{3.48}$$

and

$$\boldsymbol{K} = \boldsymbol{H}^{-1}\tilde{\boldsymbol{K}}\boldsymbol{H}^{-\mathbf{1}^{\dagger}}. \tag{3.49}$$

In Eqs. (3.48) and (3.49), $\Delta\tilde{\bar{\boldsymbol{g}}}$ and $\tilde{\boldsymbol{K}}$ are the discrete Fourier transforms (from now on referred to as DFT) of $\Delta\bar{\boldsymbol{g}}$ and $\boldsymbol{K}$, respectively. Using the general Eq. (3.7), the resulting vector of optimal frequency-based weights $\boldsymbol{w}$ will be of size $1 \times NM_xM_y$. Each entry in the $1 \times NM_uM_v$ vector of optimal weights $\tilde{\boldsymbol{w}}$, equal to the DFT of $\boldsymbol{w}$, is denoted $\tilde{\boldsymbol{w}}_{ipk}$. The $1 \times N$ sub-vector $\tilde{\boldsymbol{w}}\,(p,k)$ of $\tilde{\boldsymbol{w}}$ is equal to

$$\tilde{\boldsymbol{w}}\,(p,k) = \left(\tilde{\boldsymbol{w}}_{1pk}, ..., \tilde{\boldsymbol{w}}_{Npk}\right)^T. \tag{3.50}$$

For compactness, we drop the index m for covariance matrices and $\boldsymbol{K}$ is simply put equal to $\boldsymbol{K}^0 + \boldsymbol{K}^1$. For a wide-sense stationary random system, $\tilde{\boldsymbol{K}}$ is block-diagonal. Each $N \times N$ diagonal entry diagonal entry $\tilde{\boldsymbol{K}}\,(p,k)$ of $\tilde{\boldsymbol{K}}$ is built up of the DFT of the covariance of bin image i and j at fixed spatial frequency coordinate indices p and k, and

$$\tilde{\boldsymbol{w}}\,(p,k) = \tilde{\boldsymbol{K}}\,(p,k)^{-1}\,\Delta\tilde{\bar{\boldsymbol{g}}}\,(p,k)\,. \tag{3.51}$$

The upper limit on the (squared) SDNR, i.e. Hotelling SDNR or detectability index d', is then equal to

$$\begin{aligned} &d'^2 = \Delta\tilde{\bar{\boldsymbol{g}}}^{\dagger}\tilde{\boldsymbol{K}}^{-1}\Delta\tilde{\bar{\boldsymbol{g}}} = \\ &\sum_p\sum_k \Delta\tilde{\bar{\boldsymbol{g}}}\,(p,k)^{\dagger}\,\tilde{\boldsymbol{K}}\,(p,k)^{-1}\,\Delta\tilde{\bar{\boldsymbol{g}}}\,(p,k)\,. \end{aligned} \tag{3.52}$$

By using the weights derived in Eq. (3.51), a scalar-valued image f whose DFT is $\tilde{f}$ with elements $\tilde{f}_{pk}$, can be formed:

$$\begin{aligned}\tilde{f}_{pk} = \quad & \tilde{\boldsymbol{w}}\left(p,k\right)^{\dagger}\tilde{\bar{\boldsymbol{g}}}^{1}\left(p,k\right) = \\ & \left(\tilde{\boldsymbol{K}}\left(p,k\right)^{-1}\Delta\tilde{\bar{\boldsymbol{g}}}\left(p,k\right)\right)^{\dagger}\tilde{\bar{\boldsymbol{g}}}^{1}\left(p,k\right) = \\ & \Delta\tilde{\bar{\boldsymbol{g}}}\left(p,k\right)^{\dagger}\tilde{\boldsymbol{K}}\left(p,k\right)^{-1}\tilde{\bar{\boldsymbol{g}}}^{1}\left(p,k\right),\end{aligned} \tag{3.53}$$

where the last step follows from $\tilde{\boldsymbol{K}}\left(p,k\right)^{-1}$ being Hermitian. $\Delta\tilde{f}_{pk}$ is then equal to

$$\begin{aligned}\Delta\tilde{f}_{pk} = \quad & \tilde{\boldsymbol{w}}\left(p,k\right)^{\dagger}\tilde{\bar{\boldsymbol{g}}}^{1}\left(p,k\right) - \tilde{\boldsymbol{w}}\left(p,k\right)^{\dagger}\tilde{\bar{\boldsymbol{g}}}^{0}\left(p,k\right) = \\ & \Delta\tilde{\bar{\boldsymbol{g}}}\left(p,k\right)^{\dagger}\tilde{\boldsymbol{K}}\left(p,k\right)^{-1}\Delta\tilde{\bar{\boldsymbol{g}}}\left(p,k\right).\end{aligned} \tag{3.54}$$

The elements $\boldsymbol{K}^{\tilde{f}}_{(pk,p'k')}$ of the covariance matrix $\boldsymbol{K}^{\tilde{f}}$ for $\tilde{f}$ are given by

$$\begin{aligned}&\boldsymbol{K}^{\tilde{f}}_{(pk,p'k')} = \left\langle\left(\tilde{f}_{pk} - \langle\tilde{f}_{pk}\rangle\right)\left(\tilde{f}_{p'k'} - \langle\tilde{f}_{p'k'}\rangle\right)^{\dagger}\right\rangle = \\ &\begin{cases}\Delta\tilde{\bar{\boldsymbol{g}}}\left(p,k\right)^{\dagger}\tilde{\boldsymbol{K}}\left(p,k\right)^{-1}\Delta\tilde{\bar{\boldsymbol{g}}}\left(p,k\right), & \text{if } (p,k) = (p',k') \\ 0, & \text{otherwise.}\end{cases}\end{aligned} \tag{3.55}$$

The (squared) detectability index is then equal to

$$\begin{aligned}&d'^{2}_{\tilde{f}} = \Delta\tilde{f}^{\dagger}\boldsymbol{K}^{\tilde{f}^{-1}}\Delta\tilde{f} = \\ &\sum_{p}\sum_{k}\Delta\tilde{\bar{\boldsymbol{g}}}\left(p,k\right)^{\dagger}\tilde{\boldsymbol{K}}\left(p,k\right)^{-1}\Delta\tilde{\bar{\boldsymbol{g}}}\left(p,k\right),\end{aligned} \tag{3.56}$$

which is identical to the Hotelling-SDNR derived in Eq. (3.52).

Since

$$\tilde{f}_{pk} = \tilde{\boldsymbol{w}}\left(p,k\right)^{\dagger}\tilde{\bar{\boldsymbol{g}}}^{1}\left(p,k\right) = \sum_{i}^{N}\tilde{w}^{\dagger}_{ipk}\tilde{\bar{g}}^{1}_{ipk}, \tag{3.57}$$

we may by introducing the notation $\tilde{w}_i$ and $\tilde{\bar{g}}^1_i$ for the $M_u \times M_v$ images with pixel values $\tilde{w}_{ipk}$ and $\tilde{\bar{g}}^1_{ipk}$ where $p = 1, ..., M_u$ and $k = 1, ..., M_v$, respectively, write the image $\tilde{f}$ with pixel values $\tilde{f}_{pk}$ from Eq. (3.57), as the element-wise multiplication of $\bar{\tilde{w}}_i$ (here the overbar represents the complex conjugate of $\tilde{w}_i$ and not the mean) and $\tilde{\bar{g}}^1_i$:

$$\tilde{f} = \sum_{i}^{N}\bar{\tilde{w}}_i\tilde{\bar{g}}^1_i. \tag{3.58}$$

By taking the inverse DFT of Eq. (3.58), we obtain the optimally weighted image f in the spatial domain:

$$f = \sum_{i}^{N}\boldsymbol{H}^{-1}\bar{\tilde{w}}_i * \boldsymbol{H}^{-1}\tilde{\bar{g}}^1_i, \tag{3.59}$$

where $*$ is the convolution operator. Frequency-based weighting is thus equal to summing filtered bin images in the spatial domain, and the optimal frequency-based weights that maximize the detectability index are given by Eq. (3.51).

Application to spectral projection imaging

By using a simplified model first developed in [100], the proposed method of using optimal frequency-based weights (superscript of) has been evaluated for a pulse height discriminating silicon detector with five energy thresholds and 1×1 mm^2 large detector elements [83]. The quotient of the detectability index d'^{of}, calculated using Eq. (3.56) with optimal frequency-based weights, denoted $\tilde{\boldsymbol{w}}^{\mathrm{of}}$, and the detectability index d'^{pb} calculated with pixel-based weights, denoted $\tilde{\boldsymbol{w}}^{\mathrm{pb}}$, is evaluated for 13 different sizes of cylindrical task functions, ranging from 0.05 mm to 20 mm in radius and shown in Fig. 3.2 as a function of object radius. A 28% increase in detectability index is found for high frequency objects when applying optimal frequency-dependent weights instead of pixel-based weights. Although the weights derived are optimized for projection spectral imaging, weights optimal for reconstructed CT images and projection images have been shown to result in similar

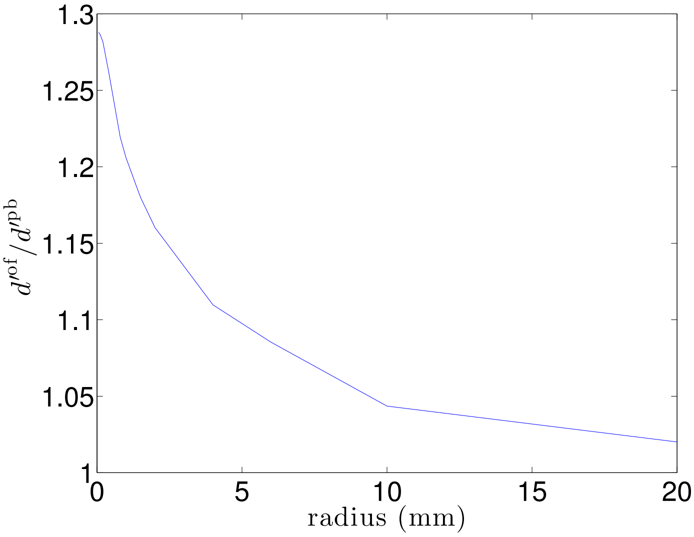

Figure 3.2: d'^{of} and d'^{pb} are the resulting detectability indices when applying optimal frequency-based weights (superscript of) and conventional pixel-based weights (superscript pb) , respectively, to the model system. Figure shows the quotient of d'^{of} and d'^{pb} as a function of object radius (mm).

SDNR under realistic noise assumptions. However, the former approach is favorable for suppressing beam hardening artifacts [50, 107].

3.3 Material basis decomposition

Spectral CT opens up for the method of material basis decomposition originally proposed by Alvarez and Macovski [51] and Macovski *et. al.* [108]. The physical basis of this method is that in the clinically relevant diagnostic energy range (e.g. between 30 to 140 keV), there are two main mechanisms of the interaction of X-rays with matter: Compton scattering (subscript Co) and photoelectric absorption (subscript ph). Since these two interactions has its own functional dependence on energy, the linear attenuation coefficient $\mu(\vec{x};E)$ of an object can be decomposed using two basis functions in the absence of K-edge discontinuities. These basis functions can be chosen as to either describe the energy dependence of Compton scattering (subscript Co) and the photoelectric effect (subscript ph), or as the mass attenuation coefficients $(\mu/\varrho)(E)$ of two materials with a large difference in atomic number Z [109]:

$$\mu(\vec{x};E) = \varrho_{Co}(\vec{x})\left(\frac{\mu}{\varrho}\right)_{Co}(E) + \varrho_{ph}(\vec{x})\left(\frac{\mu}{\varrho}\right)_{ph}(E), \tag{3.60}$$

where $\varrho(\vec{x})$ is the local density (g/cm^3). The expression in Eq. (3.60) was later adapted to allow for components exhibiting a clear K-edge (e.g. iodine or gadolinium) [109] by expanding Eq. (3.60) with one additional basis function $\varrho_k(\vec{x})\left(\frac{\mu}{\varrho}\right)_k(E)$ capturing the sudden jump in linear attenuation due to the K-edge.

In CT, the line integral of the linear attenuation coefficient $\mu\left(\vec{x};E\right)$ (cm^{-1}) is determined at each angular position and detector element (del):

$$\int \mu(\vec{x};E)\mathrm{d}s = \sum_\alpha \delta_\alpha \left(\frac{\mu}{\varrho}\right)_\alpha(E), \quad \text{for } \alpha \in \{Co, ph, k\}.$$

Above, $\delta_\alpha = \int \varrho_\alpha(\vec{x})\mathrm{d}s$ is the area density (g/cm^2) and $(\mu/\varrho)_\alpha(E)$ equal to the mass attenuation coefficient. This allows for decomposition of the projection images in three (or more) basis images.

Material basis decomposition using dual energy CT

Common for the dual energy technologies is that only two spectrally independent measurements are provided. Since an accurate material basis decomposition of an object containing a contrast agent with a K-edge requires at least three spectrally distinct X-ray measurements per projection [111], some type of prior assumption about the imaging objects attenuating characteristics must be made in order to estimate the density map using dual energy CT.

One of two methods frequently suggested for quantification of iodine [23, 112] using dual energy CT is to approximate all body materials with water and perform a material basis decomposition in the projection space [109]. The second method is based on assigning each reconstructed voxel a ratio of soft tissue and fat. Since a small addition of K-edge contrast agent to both soft tissue and fat and any mixture of those two materials leads to a similar and measurable enhancement vector [53], the amount of contrast agent can be estimated from a dual energy measurement by plotting the low (ξ_1) and high (ξ_2) measured CT-values in a HU-diagram. This method uses two body material data points defined as in Eq. (2.6), ${\xi_j}^{\mathrm{f}}$ and ${\xi_j}^{\mathrm{t}}$ for $j = 1, 2$, corresponding to fat (denoted by f) and soft tissue (denoted by t) with densities equal to ϱ_{f} and ϱ_{t}, respectively.

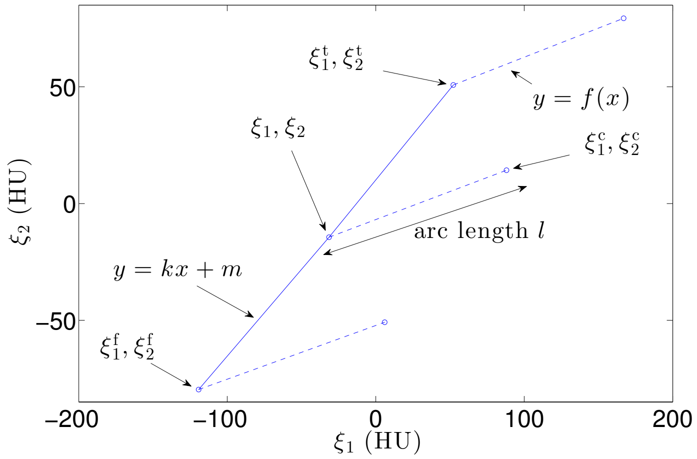

Figure 3.3: Figure illustrating the method of estimating the amount of contrast agent (superscript c) present in a voxel consisting of soft tissue (superscript t) and fat (superscript f) using dual energy CT. By plotting the low (${\xi_1}^{\mathrm{c}}$) and high (${\xi_2}^{\mathrm{c}}$) measured CT-values in a HU-diagram where the line $y = kx+m$ describes CT values for any mixture of soft tissue and fat, the contrast agent density (proportional to the arc length l) can be calculated using the enhancement function $y = f(x)$.

By drawing a line between the points $(x, y) = \left({\xi_1}^{\mathrm{f}}, {\xi_2}^{\mathrm{f}}\right)$ and $(x', y') = ({\xi_1}^{\mathrm{t}}, {\xi_2}^{\mathrm{t}})$ as illustrated in Fig. 3.3, the high energy CT-value ξ_2 of any mixture of soft tissue and fat without the presence of a K-edge material can be written as $\xi_2 = k\xi_1 + m$, where ξ_1 is the low energy CT-value,

$$k = \frac{{\xi_2}^{\mathrm{t}} - {\xi_2}^{\mathrm{f}}}{{\xi_1}^{\mathrm{t}} - {\xi_1}^{\mathrm{f}}}, \tag{3.61}$$

and

$$m = {\xi_2}^{\mathrm{f}} - k{\xi_1}^{\mathrm{f}}. \tag{3.62}$$

If the attenuating object contains some amount of contrast agent (denoted by c), the high and low energy measurements ${\xi_2}^{\mathrm{c}}$ and ${\xi_1}^{\mathrm{c}}$ will no longer be located along the line $y = kx + m$. By successively adding a small amount of contrast agent to a mixture of fat and soft tissue, the enhancement function $y = f(x)$ at every point along the line $y = kx + m$ and a function $g(l)$, where an arc length l corresponds to a contrast agent density ϱ_{c}, can be calculated.

Material basis decomposition using a photon counting multiple-bin detector

While dual energy integrating CT is based on performing two spectrally distinct measurements for each exposure, multiple-bin photon counting systems measure the energy of each photon using a single spectrum and a number of energy bins. For a photon counting detector with N bins, the registered counts in each bin B_i, denoted $m_i(x')$ where $i = 1, ..., N$, is used to determine the line integrals δ_α by solving the system of integral equations for δ_α:

$$m_i(x') = I_0(x') \int_\Phi \Phi(E) D(E) S_i(E) \mathrm{e}^{-\sum_{\alpha=1}^{m} \delta_\alpha \left(\frac{\mu}{\varrho}\right)_\alpha (E)}, \quad i = 1,..., N.$$

Above, $I_0(x')$ is the total number of photons impinging on the area of the object projected onto the detector element at x' during the projection image acquisition time. We define a bin function $S_i(E)$ according to the notation in [66] using the Heaviside step function $\chi(x)$, being 1 for $x \geq 0$ and zero otherwise:

$$S_i(E) = \chi(E - T_i) - \chi(E - T_{i+1}). \tag{3.63}$$

In Eq. (3.63), T_i for $i = 1, ..., N$ are the energy thresholds such that events with energy E are placed in bin B_i if $T_i \leq E < T_{i+1}$. $D(E)$ is the detection efficiency of the detector and $\Phi(E)$ the X-ray spectrum on the target designed such that the fraction of X-rays with energy in the interval $(E, E + \mathrm{d}E)$ is given by $\Phi(E)\mathrm{d}E$. As long as the number of bins is larger than two, an unbiased estimation of the amount of contrast agent in any object can be made using a material basis decomposition method either in image space [113–116] or in projection space [55,65,109], requiring knowledge of the incident spectrum, or alternatively by using a calibration phantom as suggested in the work by Alvarez [110].

3.3.1 Quantification of material basis decomposition accuracy

Mean square error

An unbiased estimator is an estimator that on average will yield the true value of the unknown parameter θ [117]:

$$\mathbb{E}(\hat{\theta}) = \theta \quad a < \theta < b, \tag{3.64}$$

where (a, b) denotes the range of possible values of θ, and $\mathbb{E}$ denotes the expectation value. The bias of the estimator of θ, denoted $\text{bias}_{\hat{\theta}}$, is defined as:

$$\text{bias}_{\hat{\theta}} = \mathbb{E}(\hat{\theta}) - \theta. \tag{3.65}$$

A figure of merit that takes into account both of the variance and the bias defined above is the mean square error (MSE):

$$\text{MSE}_{\hat{\theta}} = \mathbb{E}[(\hat{\theta} - \theta)^2]. \tag{3.66}$$

The MSE measures the difference between the estimator and what is estimated. It can be rewritten as

$$\begin{aligned} \text{MSE}_{\hat{\theta}} &= \mathbb{E}\Big[\Big(\hat{\theta} - \theta\Big)^2\Big] = \Big(\mathbb{E}[\hat{\theta}^2] - \mathbb{E}[\hat{\theta}]^2\Big) + \\ & \Big(\mathbb{E}[\hat{\theta}] - \theta\Big)^2 = {\sigma_{\hat{\theta}}}^2 + {\text{bias}_{\hat{\theta}}}^2, \end{aligned} \tag{3.67}$$

where ${\sigma_{\hat{\theta}}}^2$ is the variance of the estimator. For an unbiased estimator, the MSE is equal to the variance.

Cramér-Rao lower bound

The Cramér-Rao lower bound (CRLB) expresses a lower bound on the variance of any unbiased estimator [117]. Since no unbiased estimator can be found that yields a lower variance, it provides an efficient benchmark against different unbiased estimators can be compared [111, 117]. For the unbiased estimate $\hat{\boldsymbol{\theta}}$ of a parameter vector $\boldsymbol{\theta} = [\theta_1 \theta_2 ... \theta_p]^T$, the lowest variance $\sigma^2_{\hat{\theta}_i}$ of the estimate of parameter θ_i, is equal to element $[i, i]$ of the inverse of the so called *Fischer* matrix $\boldsymbol{I}(\boldsymbol{\theta})$:

$$\sigma^2_{\hat{\theta}_i} \geq [\boldsymbol{I}^{-1}(\boldsymbol{\theta})]_{ii}, \tag{3.68}$$

where

$$[\boldsymbol{I}^{-1}(\boldsymbol{\theta})]_{ij} = -\mathbb{E}\Big[\frac{\partial^2 \ln p(\boldsymbol{x}; \theta)}{\partial \theta_j \partial \theta_j}\Big] \tag{3.69}$$

for $i = 1, 2, ..., p$ and $j = 1, 2, ..., p$ where $p(\boldsymbol{x}; \theta)$ is the probability density function of the data.

Comparison between material basis decomposition performed using dual energy CT and a photon counting multiple-bin detector

For any K-edge material basis decomposition method using dual energy CT, the quantification of contrast agent will be unbiased for objects corresponding to the prior assumption (e.g. of being composed of solely water and iodine, or a mixture of soft tissue, fat and contrast agent), and a lowest variance for such an estimation can be calculated using the CRLB [117–119]. For any object not satisfying the condition, the estimation of contrast agent content will be biased.

Wang and Pelc [118] simulated an optimized dual energy CT system and estimated the minimum variance of contrast agent estimation using the CRLB for an object consisting of water and iodine. The result was compared to the minimum variance using a photon counting multiple-bin detector with optimized settings, taking into account a limited energy resolution, pileup and spectrum tailing. The results indicated that the performance of a typical photon counting detector could be compared to using an optimized dual kV system. Following the work of Wang and Pelc [118], Bornefalk and Persson [119] compared the theoretical limits of iodine quantification for ideal dual energy and multi-bin systems using a common input spectrum for both technologies. In that work, the CRLB was used to assess the standard deviations of unbiased iodine content estimations where both systems were allowed to make prior correct assumptions about the densities of the two composing materials soft tissue and fat.

A patient being imaged however rarely consists of solely water and contrast agent, or for that matter soft tissue, fat and contrast agent. When comparing an actual proposed and implemented method of contrast agent quantification using dual energy CT to the performance of a photon counting multiple-bin detector, the inherent risk of model specification error using dual energy CT should be taken into account. Since it is not possible to have complete knowledge about the elemental composition of a voxel by forehand, such a risk is always present. One clinical example of this is the presence of plaque in a blood vessel, another a piece of bone filling up a certain portion of the voxel. By using the MSE (which includes the bias and not solely the variance) as a figure of merit, the uncertainty accompanying making prior, possibly false, assumptions about the object can be quantified.

In Fig. 3.4a, an example of the square root of the MSE in contrast agent quantification using an optimized dual energy system (superscript dual) subject to dose and power constraints is shown for a voxel consisting of soft tissue, fat and iodine (subscript I). The method of contrast agent content estimation based on assigning each reconstructed voxel a ratio of soft tissue and fat, described in Sec. 3.3, was applied and the square root of the MSE estimated using propagation of errors. In the same figure, the square root of the MSE in contrast agent quantification calculated using the CRLB for the same object using an optimized photon counting multiple-bin silicon detector (superscript pc), also subject to dose and power constraints, is shown. For both systems, the detector element sizes are 1×1 mm^2. As can be seen, the square root of the MSE for an object consisting of only soft tissue, fat and contrast agent (corresponding to the prior assumptions which means that the bias is zero for the dual energy system) results in a smaller square root of the MSE using dual energy CT compared to using a multiple-bin detector.

In Fig. 3.4b, the square root of the MSE for the same systems are shown for the contrast agent content estimation in a voxel consisting of soft tissue, fat, iodine and a 2.2% voxel volume fraction of bone. By adding a small amount of bone, the square root of the MSE for small concentrations of contrast agent using the dual energy system is approximately twice as large as the square root of MSE using a photon counting multiple-bin detector. The increase in MSE using a dual energy system is due to the bias introduced by adding small amounts of a material not included in the prior assumptions. The result indicate that using a spectrally resolved detector where the number of energy bins is larger than two reduces the risk of introducing a bias in contrast agent content estimation when performing a material basis decomposition. This is something that cannot be neglected for a dual energy CT system since it in reality is impossible to have complete knowledge about the elemental composition of a voxel by forehand.

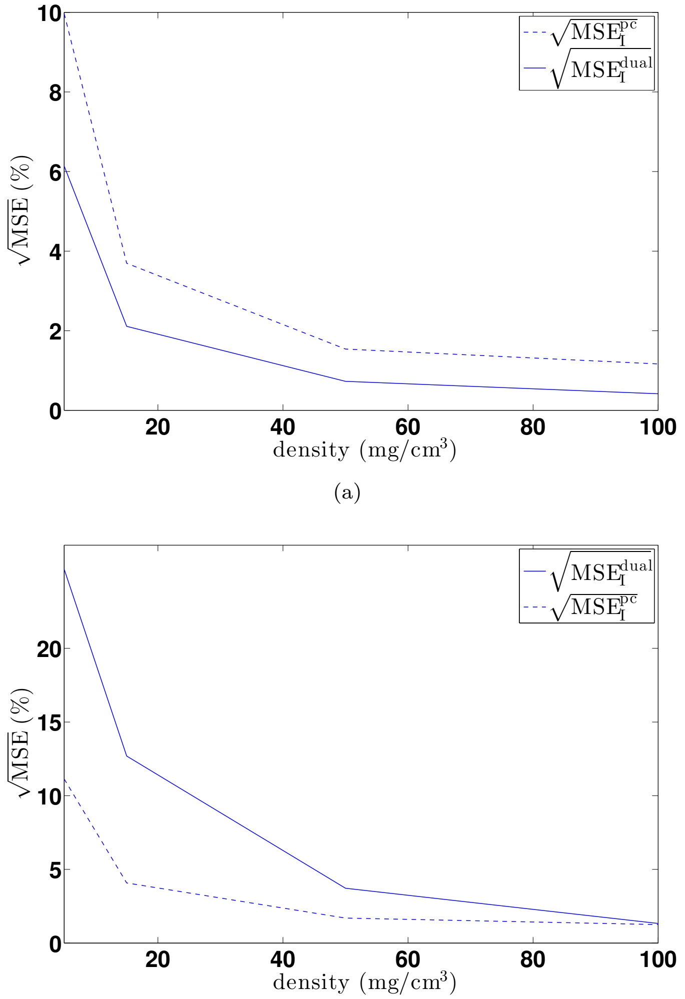

(a)

(b)

Figure 3.4: Figs. 3.4a and 3.4b show the square root of the MSE of the contrast agent content estimation using dual energy CT (superscript dual) and the square root of the MSE of the unbiased contrast agent content estimation using a multi-bin silicon detector (superscript pc), as a function of iodine content ϱ (mg/cm^3), respectively. The square root of the MSE is evaluated in percentage of iodine (subscript I) content ϱ. In Fig. 3.4a, the object consists of soft tissue and fat. In Fig. 3.4b, the object consist of soft tissue, fat and bone where the amount of bone is specified by percentage of bone volume per total voxel volume, equal to 2.2%.

Chapter 4

Measurements of detector performance

During the past few years, various methods of measuring DQE have been established, making the comparison of DQE values difficult. In 2003, the IEC62220-1 standard was introduced to standardize DQE measurements, including specifications for the measurement of the MTF and the NPS. While this standard addresses radiography where the image is directly related to the detection performance, thus excluding CT, it can still be useful to quantify the three-dimensional DQE [20] as well as the two-dimensional projection DQE [120] for CT systems.

Below, methods of measuring the projection pre-sampling MTF and projection NPS from single-view projection measurements are briefly reviewed. It should be noted that measuring the three-dimensional MTF and NPS from reconstructed CT images differ from these procedures [20].

4.1 MTF

The line-spread function (lsf) describes the response of the system to a “line” delta function, which for shift-invariant systems can be written as [72]

$$\mathrm{lsf}(x) = \frac{\int_{-\infty}^{\infty} \mathrm{psf}(x,y)\mathrm{d}y}{\int_{-\infty}^{\infty}\int_{-\infty}^{\infty} \mathrm{psf}(x,y)\mathrm{d}y\mathrm{d}x}. \tag{4.1}$$

The one-dimensional MTF is then equal to

$$\mathrm{MTF}(u) = |\mathcal{F}\{\mathrm{lsf}(x)\}|. \tag{4.2}$$

In practice, a digital systems over-scanned line spread function can be measured by recording the response in a single detector element while moving a thin slit along the direction in which the pre-sampling projection MTF is to be estimated [121, 122].

Another alternative is to use an edge test device and measure the systems edge-spread function from which the line-spread function can be calculated by differentiation [122].

4.2 NPS

Measurements of the projection NPS can be performed by acquiring a large number of uniformly exposed projection (i.e. single view) measurements. Ideally, a centre region in the projections should be divided into smaller regions of interest (ROI) $I(x, y)$ of size $N_x \times N_y$. For each ROI, a two-dimensional sample noise power spectrum is calculated by the Fourier transform. Averaging of the individual spectra then yields the two-dimensional digital noise spectrum (see e.g. [72, 123]):

$$\mathrm{NPS}_{dig}(u, v) = \frac{a_x a_y}{N_x N_y} \mathbb{E} \left\{ \left| F \left\{ \Delta I(x, y) \right\} \right|^2 \right\}, \tag{4.3}$$

where $\Delta I(x, y) = I(x, y) - \mathbb{E}\{I(x, y)\}$. In Eq. 4.3, a_x and a_y are the dimensions of the detector element size in the x- and y-direction, respectively. The one-dimensional NPS for a 2-dimensional process is calculated as

$$\mathrm{NPS}_{dig}(u) = \frac{a_x a_y}{N_x N_y} \mathbb{E} \left\{ \left| F \left\{ \sum_{y=1}^{N_y} \Delta I(x, y) \right\} \right|^2 \right\}, \tag{4.4}$$

and the NPS for a 1-dimensional process as

$$\mathrm{NPS}_{dig}(u) = \frac{a}{N} \mathbb{E} \left\{ \left| F \left\{ \Delta I(x) \right\} \right|^2 \right\}. \tag{4.5}$$

In Eq. (4.5), it is assumed that one-dimensional projection images $I(x)$ of size $1 \times N$ are acquired and that the detector element size is a along the x-direction.

4.3 DQE of photon counting silicon detector

The Physics of Medical Imaging group at KTH is developing a photon counting multiple-bin detector for clinical CT [28, 124–126]. The detector is fabricated on a high resistivity n-type silicon substrate and consists of wafers pointing back to the radiation source in an edge-on geometry. Each silicon wafer is 0.5 mm thick in the x-direction, and the depth of each wafer is approximately 30 mm to provide a high detection efficiency for high-energy X-rays in clinical CT applications. The active area of each wafer extends 20 mm in the y-direction, and is segmented by means of 50 rows of collection electrodes yielding a pitch of 0.4 mm. Consequently, the detector pixel size is equal to 0.5×0.4 mm^2, and the number of slices per rotation equal to 50. Each wafer is segmented along the direction of the incident X-ray photons into 9 depth segments with exponentially increasing lengths to ensure a

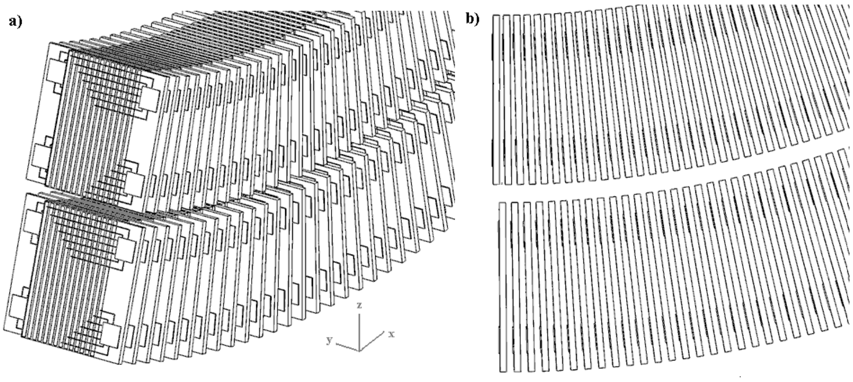

Figure 4.1: Basic layout of the detector. Photons impinge in the direction $(0, 0, -1)$. Panel (a) shows how the silicon wafers are stacked in two planes and how the detector elements extends in the rotational (x-) direction, pointing back to the X-ray source. Panel (b) is a collapsed view of the x, z-plane showing the spacing between wafers, necessary for cooling and electronic circuitry, and also how the lower level of detector wafers is offset with one pixel width in the x-direction.

uniform count rate over all segments. As a result, the count rate in each detector segment is reduced. Each depth segment has individual charge sensing channels connected to an electronic readout channel in the application specific integrated circuits (ASIC) bonded directly to the silicon substrate. Following an X-ray interaction in the detector, the ASIC amplifies and shapes the current pulse produced. The pulse height (which is proportional to the amount of energy deposited) is then counted by one of the eight energy bins formed by eight adjustable energy thresholds. To absorb scattered radiation in the detector in the x-direction, each detector wafer is backed with a thin foil (30 μm thick) consisting of a commercially available tungsten-compound. To provide space for electronic circuits and enable cooling, the detector modules are stacked in two layers as illustrated in Fig. 4.1. The tungsten sheats are extended by 2.5 cm pointing towards the source, thereby acting as a 1-dimensional object scatter grid. The full CT detector consists of approximately 2000 number of wafers, adding up to a total detector length of roughly 80 cm.

In november 2104, four silicon wafers were successfully installed in a Philips iCT gantry (Fig. 4.2), providing a 2×20 mm^2 large detector configuration composed of $4{\times}50$ detector elements. For this prototype, no tungsten shielding was included and the source-to-detector and source-to-isocenter distances were equal to 1040 mm and 570 mm, respectively.

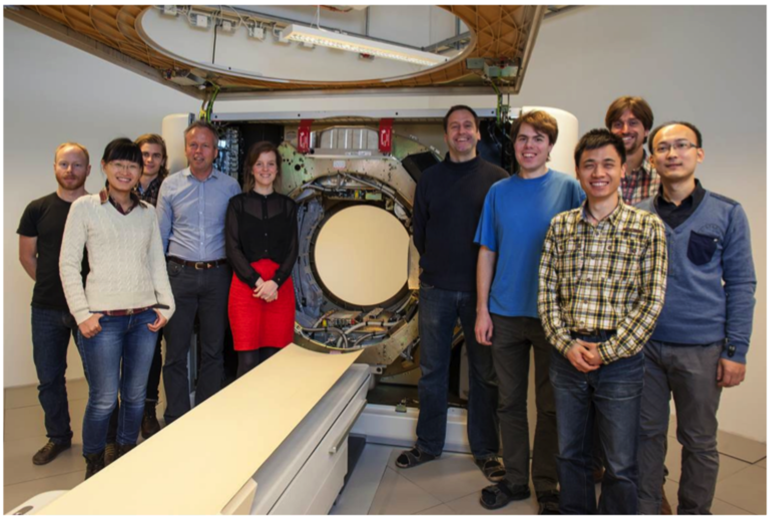

Figure 4.2: Part of Physics of Medical Imaging group at KTH in front of Philips iCT gantry in which the first silicon wafers successfully were installed in november 2014.

4.3.1 MTF

Measurements of the 1-dimensional pre-sampling projection MTF in the y-direction, sometimes referred to as the *longitudinal* MTF, for the wafers installed in the gantry were performed by scanning a thin slit source of X-rays and taking the Fourier transform. The narrow slit of X-rays was constructed by placing two 13 mm thick rectangular blocks of tungsten 20 μm apart approximately 10 cm above the detector surface. The slit was aligned along the x-direction and could be moved along the y-direction with small steps using a linear stage. The tube peak voltage was equal to 80 kVp and the spectrum was filtered with 5 mm of aluminum. The response in a single detector element was recorded while the slit was moved with a step size equal to approximately 10 μm at the detector plane, providing the over-scanned line-spread function in the y-direction from which the pre-sampling projection MTF was calculated by taking the Fourier transform. At the time of measurement, depth segment nine was corrupted by an unknown noise source later identified as electronic noise originating from surrounding components transferred via a connecting wire. For the calculation of the MTF, segment nine was subsequently not used, and the lowest threshold was put quite high (approximately 16 keV) to remain above the noise floor.

The MTF resulting from measurements was compared to previously performed Monte Carlo simulations of the pre-sampling projection MTF [127]. In the simulation, a 6.5 cm long (in the x-direction) times 2 cm wide (in the y-direction) detector was modeled and the interaction locations of 10^6 number of photons impinging uniformly onto the center detector element were recorded, together with the deposited energies. The primary energies were drawn from a simulated spectrum [46] with a peak voltage of 80 kVp, filtered with 3 mm of aluminum and 0.1 mm of copper using linear attenuation coefficients from [43]. In the simulations, a 30 μm thick tungsten shielding was modeled, covering the backside of each wafer. Charge sharing was not included in the simulation model and the energy bins were equidistantly placed with the lowest energy threshold at 5 keV.

The measured over-scanned line-spread function and resulting pre-sampling projection MTF are shown in Figs. 4.3a and 4.3b, together with the pre-sampling projection MTF generated from simulations. For both the measurement and simulation, photon counting weights were applied. Note that the spatial frequency axis of the MTF is referenced to the isocenter of the CT scanner. To reference it to the detector plane it should be scaled by 570 mm/1040 mm.

4.3.2 NPS

10 000 uniformly exposed projection images with a frame rate of 5 000 frames per second (fps) were acquired. For the measurements, a 30 cm thick water phantom was placed between the X-ray source and prototype detector. At the time of measurement, only one silicon wafer was accessible for recording and transmitting signal. The output data was therefor 1-dimensional of size 1×50, corresponding to 50 detector elements in the y-direction. To estimate the projection NPS, the formula in Eq. (4.5) for calculating the 1-dimensional NPS from 1-dimensional data was subsequently applied even though the prototype detector in practice is 2-dimensional. The tube peak voltage was equal to 80 kVp filtered with 5 mm of aluminum and the tube current was equal to 500 mA. As for the MTF measurements, depth segment nine was corrupted by an (at the time) unknown noise source and subsequently not used. The energy bins were equidistantly placed with the lowest energy threshold at approximately 16 keV.

4.3.3 DQE

The 1-dimensional projection DQE using photon-counting weights (i.e. weighing all bins identically) was calculated according to Eq. (3.34) using the 1-dimensional pre-sampling OTF and the 1-dimensional projection NPS in the y-direction acquired from measurements in the gantry:

$$\mathrm{DQE}(u) = \frac{\left|\sum_i^N w_i N_{\ i} \mathrm{OTF}_i\,(u)\right|^2}{\mathrm{NPS}\,(u) \sum_i^N q_{\ i}}. \tag{4.6}$$

In Eq. (4.6), $N_{\ i}$ is equal to the average number of detected photons in bin i . The input number of counts per detector element, $\sum_i^N q_{\ i}$, was estimated by measuring the air kerma rate (mGy/mAs) using an ionization chamber (Unfors Instruments

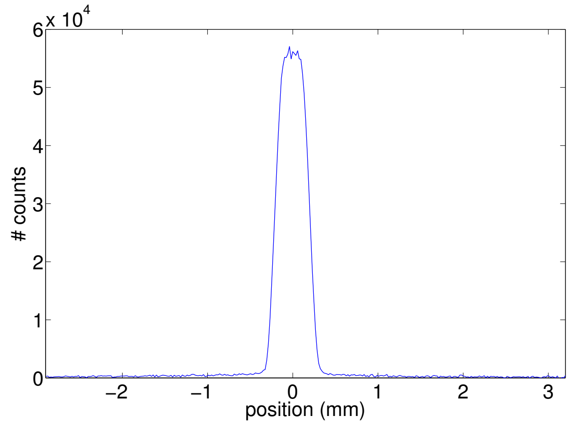

(a) Measured line-spread function.

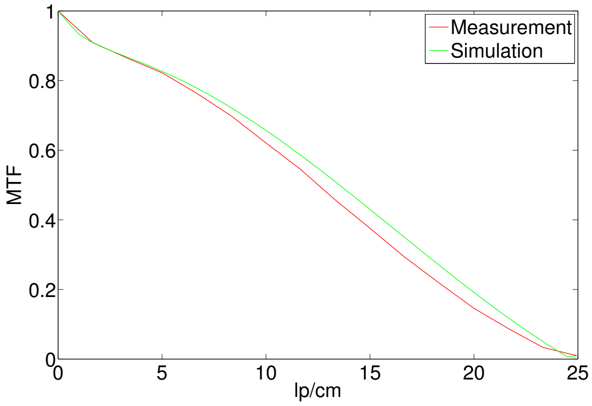

(b) MTF resulting from measurements and simulations.

AB, Billdal, Sweden). A simulated spectrum [46] was used in combination with data from the work of J. Boone and J. Seibert [128] for the translation from mGy/mAs to photon fluence (photons/mm^2 $\cdot$ s).

The 1-dimensional projection DQE resulting from measurements was compared to the 1-dimensional projection DQE estimated using previous Monte Carlo simulations of the detector [127]. To estimate the projection NPS, 200 projection image matrices of size 50×80 were generated using a simulated spectrum [46] with a peak voltage of 80 kVp filtered with 3 mm of aluminum and 0.1 mm of copper [43]. The 2-dimensional projection NPS was calculated according to Eq. (4.3), from which the 1-dimensional projection NPS was computed using Eq. (3.24). In the simulations, a 30 μm thick tungsten shielding was modeled, covering the backside of each wafer. Charge sharing was not included in the simulation model and the lowest of the eight equidistantly placed energy bins was equal to 5 keV. Next, the one-dimensional projection DQE from simulation was estimated according to Eq. (3.34), using the OTF acquired from simulations as described above in Sec. 4.3.1.

The results of the measurements are presented in Fig. 4.4, together with the projection DQE estimated from simulations of the detector at identical kVp settings using photon counting weights. The spatial frequency axis of the DQE is referenced to the the isocenter of the CT scanner.

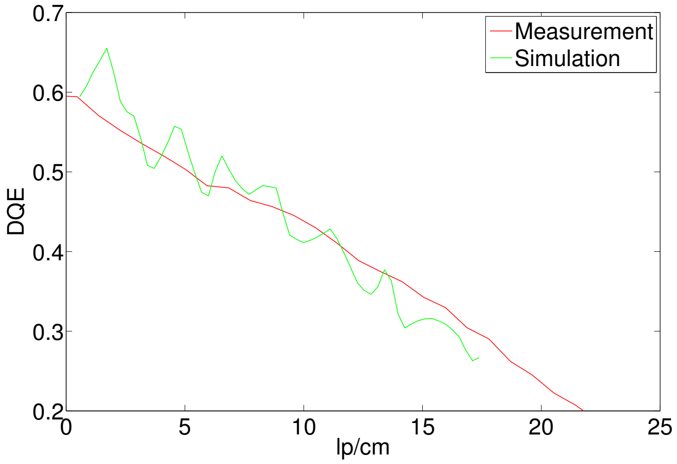

Figure 4.4: Measured and simulated projection DQE in y-direction.

4.3.4 Electronic noise

Two distinct types of image noise that limit the detectability and interfere with the interpretation of a CT image [129] are statistical and electronic noise. The source of statistical noise is the fluctuations inherent in the detection of a finite number of X-ray quanta, commonly denoted quantum noise. It represents a fundamental limitation in the X-ray imaging process and can only be reduced by increasing the detected number of quanta. This can be done by developing more efficient detectors, or by increasing the transmitted dose (e.g. mAs). Electronic noise is the random fluctuations in electrical signals that comes from electronic components in the X-ray detection system [130]. Since conventional CT detectors integrate the total electrical current, charges resulting from both X-ray detection and electronic noise are summed. For such detectors, measurements free from contribution of electronic noise is not possible to obtain since the two types of events can not be separated.

For a regular CT scan, the measurement noise is dominated by quantum noise rather than electronic noise. At low dose settings however, the electronic noise may become a dominant factor limiting the image quality. This effect is illustrated in the work by Luhta *et al.* [131], who measured the projection DQE for an energy integrating detector as a function of dose. The results demonstrate a zero-frequency DQE that is constant and equal to approximately 0.75 for dose rates ranging between 200 mR/s and 2.2 mR/s. When decreasing the dose rate to 0.28 mR/s however, the zero-frequency DQE drop to 0.4. A dose rate equal to 0.028 mR/s, results in a zero-frequency DQE equal to 0.1, implying that the electronic noise is the principal source of noise. Using pulse height discriminating photon counting detectors, proper settings of the low energy threshold can effectively reject electronic noise. This opens up for low-dose imaging, important especially for pediatric imaging tasks.

Measurement of projection DQE as a function of dose

The 1-dimensional projection NPS was calculated from measurements using a single silicon wafer installed in a table-top-setup. For calculations of the NPS, 10 000 frames were acquired for a frame rate of 31250 fps at seven different exposures (i.e. mA) ranging from 0.5 to 5 mA and a tube voltage equal to 80 keV. The spectrum was filtered with 4 mm of aluminum. The resulting zero-frequency DQE is presented in Fig. 4.5. For these measurements, the lowest threshold was put at approximately 10 keV and the following energy bins equidistantly placed. The input number of counts q per detector element was estimated by measuring the air kerma rate (mGy/mAs) using an ionization chamber (Unfors Instruments AB, Billdal, Sweden). As described in Sec. 4.3.3, a simulated spectrum [46] was used in combination with data from the work of J. Boone and J. Seibert [128] for the translation from mGy/mAs to photon fluence (photons/mm^2 $\cdot$ s). As can be seen in Fig. 4.5, the DQE at zero frequency is approximately constant, implying that the electronic noise is negligible down to 16 μAs.

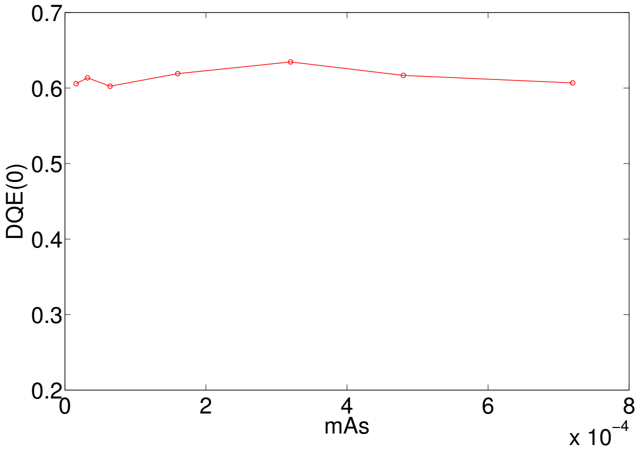

Figure 4.5: Measured DQE(0) as a function of mAs and a tube voltage equal to 80 keV.

Chapter 5

Summary of the appended papers

5.1 Paper A: Performance evaluation of a sub-millimeter spectrally resolved CT system on high- and low-frequency imaging tasks: a simulation

Paper A is co-authored with Mats Danielsson and Hans Bornefalk and is published in *Physics in Medicine and Biology*, Vol. 57, No. 8, pp. 2373-2391, 2012.

The purpose of Paper A is to incorporate the spatial frequency dependence of signal and noise when comparing the performance of a proposed photon counting detector to an energy integrating system. This is done by reconstructing the 3D MTF and NPS of a silicon strip detector with 0.5×0.4 mm^2 large detector elements using cascaded system analysis. The reconstructed noise and signal characteristics are compared with a reconstructed 3D MTF and NPS of an ideal energy-integrating detector system with unity detection efficiency, no scatter or charge sharing inside the detector, unity pre-sampling MTF and 1×1 mm^2 detector elements.

The dose-normalized detectability index d' is calculated for four different imaging tasks. Results indicate that for imaging of high-frequency objects, d' using the proposed silicon detector is 110-130% of the detectability index obtained using an ideal energy-integrating system. For low-frequency objects, the improvement in the reconstruction of the linear attenuation coefficients using projection-based weighting in combination with the smaller detector element size results in a dose-normalized detectability index of the silicon detector that is 105-110% of an ideal energy-integrating system.

5.2 Paper B: Eliminated risk of iodine contrast cancellation with multibin spectral CT

Paper B is co-authored with Mats Persson, Joakim Crafoord, Mats Danielsson and Hans Bornefalk and is published in *Physics in Medicine and Biology*, Vol. 58, No. 14, pp. 201-209, 2013.

In this paper, the extent of contrast cancellation induced by iodinated contrast agents in energy integrating and photon counting multiple-bin CT images is considered. The contrast-to-noise ratio of a hypodense tumor filled with successively increasing amount of iodine against a homogenous background composed of liver tissue is modeled for the two systems for a range of iodine concentrations and tube voltages. For the energy integrating systems, the contrast between the target and the background vanishes for iodine concentrations around 2–6 mg I/ml, dependent on tube voltage. Although the contrast-to-noise ratio for each tube voltage has a minimum for a certain iodine concentration, this effect is absent for the multiple-bin systems due to the capability to utilize any local difference in the attenuation coefficients to generate contrast in the final image by means of energy weighting.

5.3 Paper C: Theoretical comparison of a dual energy system and photon counting silicon detector used for material quantification in spectral CT

Paper C is co-authored with Mats Danielsson and Hans Bornefalk and is published in *IEEE Transaction on Medical Imaging*, Vol. 34, No. 3, pp. 796-806, 2014.

In this paper, a frequently suggested method for material basis decomposition using dual energy CT, based on assigning each reconstructed image voxel a ratio of fat and soft tissue with fixed densities, is evaluated. The purpose is to compare the ability of a dual energy CT system to estimate the amount of iodine and gadolinium that are present in an object to that of a photon counting multiple-bin silicon detector. For both systems, the tube voltages, filtrations and currents are optimized subject to dose and power constraints.

The results of this work suggest that when only two materials with known densities are present in the enhancing voxel, the noise levels of the unbiased iodine and gadolinium content estimations using the silicon detector are higher than the noise levels of the unbiased iodine and gadolinium content estimations using a dual energy system. However, using a spectrally resolved detector where the number of energy bins is larger than two reduces the risk of introducing a bias in contrast agent content estimation when performing a material basis decomposition, something that cannot be neglected for a dual energy CT system since it in reality is impossible to have complete knowledge about the elemental composition of a voxel by forehand.

5.4 Paper D: Optimal frequency-based weighting for spectral X-ray projection imaging

Paper D is co-authored with Mats Persson and Hans Bornefalk and is published in *IEEE Transaction on Medical Imaging*, 34(3), pp. 779 - 787, 2014.

In paper D, a novel frequency-based weighting scheme which provides the upper limit on the frequency-based SDNR (detectability index d') for spectral projection imaging is presented. In comparison to pixel-based weighting, the method allows for taking into account each frequency component in a certain bin and is particularly beneficial for systems with complex correlation structures.

The frequency-based signal and noise for a spectrally resolved photon counting detector with N bins acquiring two-dimensional projection bin images are defined. Optimal frequency-based weights are calculated and it is shown that frequency-based weighting is equal to summing filtered bin images in the spatial domain. The detectability indices for 13 different sizes of cylindrical task functions with radius ranging from 0.05 mm to 20 mm are calculated using optimal frequency-based weights and compared to the detectability indices obtained when applying conventional pixel-based weights. The maximum gain achievable using frequency-based weights is equal to 1.28 for the smallest radius and drops towards 1 for the largest radius.

5.5 Contribution by co-authors

For papers A, B and C, Hans Bornefalk and Mats Danielsson acted as advisors and supervisors of the work. The reconstructed CT image of a PMMA phantom taken with a clinical energy integrating CT system at the Karolinska University hospital in paper A was provided by Joakim Crafoord. Mats Persson contributed with valuable discussions and suggestions for the research on which paper B and D are based. For paper D, Hans Bornefalk acted as supervisor.

Acknowledgements

First and foremost I want to express my special appreciation and thanks to two people: Prof. Mats Danielsson for giving me the opportunity of finishing a PhD whilst being part of an exciting (and fun!) project, and my supervisor Hans Bornefalk who made this work possible by always being available for discussion and advice. There is no overstatement in concluding that without your guidance, this thesis would not have been completed.

I also want to thank present and past members of the Physics of Medical Imaging group at KTH. Apart from providing a great work environment, you have contributed substantially to the finalizing of this thesis by helping and supporting me during my years as a PhD. Special thanks go out to Mats Persson for valuable advice and discussions regarding practically all of my work but especially paper D; Cheng Xu and Ben Huber for help with Monte Carlo simulations; Staffan Karlsson for help with mechanics; Martin Sjölin and Fredrik Grönberg for writing the code used for the measurements of the MTF and NPS, and also for performing the measurements in the CT gantry and table-top setup.

Last but not least, I also want to thank my family and especially my parents, Lena and Anders, for always being there and supporting me in every possible way, Mattias for understanding even though you don’t, and Liv for putting things in the right perspective. I love you all.

Bibliography

[1] Walter J. Savitch. *Pascal: An Introduction to the Art and Science of Programming* Benjamin/Cummings Publishing Co. Inc. Redwood City, CA, USA, 1986.

[2] *Nobel Lectures, Physics 1901-1921*, Elsevier Publishing Company, Amsterdam, 1967.

[3] J. Radon,Ürber die Bestimmung von Funktionen durch ihre Integralwerte längs gewisser Mannigfaltigkeiten, Berichte Sächsische Akademie der Wissenschaften, Leipzig, Math.-Phys. Kl., 69, 262-267.

[4] A. M. Cormack and G. N. Hounsfield. "1979 A M Cormack and G N Hounsfield" in *Nobel Lectures in Physiology or Medicine 1971-1980*, J. Lindsten, Ed. (Karolinska Institutet, Stockholm), World Scientific Publishing Company, Singapore, 1992.

[5] W. A. Kalender. *Computed tomography: Fundamentals, System Technology, Image Quality, Applications.* John Wiley & Sons, New York, 2005.

[6] W. Lee and J. Goldman. Principles of CT and CT Technology. *J. Nucl. Med. Technol.*, 35(3): 115-128, 2007.

[7] B. Heismann, B. T. Schmidt and T. G. Flohr. *Spectral computed tomography.* SPIE press, Bellingham, Washington, USA, 2012.

[8] Y. Murai, R. Takagi, Y. Ikeda, Y. Yamamoto and A. Teramoto. Three-dimensional computerized tomography angiography in patients with hyperacute intracerebral hemorrhage. *J. Neurosurg.*, 91:424-431, 1999.

[9] R. Wada, R. I. Aviv, A. J. Fox, D. J. Sahlas, D. J. Gladstone, G. Tomlinson and S. P. Symons. CT angiography "spot sign" predicts hematoma expansion in acute intracerebral hemorrhage. *Stroke*, 38:1257-1262, 2007.

[10] J. N. Goldstein, L. E. Fazen, R. Snider,K. Schwab, S. M. Greenberg, E. E. Smith, M. H. Lev and J. Rosand. Contrast extravasation on CT angiography predicts hematoma expansion in intracerebral hemorrhage. *Neurology*, 68:889-894, 2007.

[11] X. L. Li, F. M. Zhou, S. Q. Shangguan, W. Q. Zou, Y. Q. Deng, T. Chen and G. H. Chen. Application of computed tomography for differential diagnosis of glioma stoke and simple cerebral hemorrhage. *Asian Pac. J. Cancer Prev.*, 15(8):3425-3428, 2014.

[12] M. Prokop and M. Galansk. *Spiral and Multislice Computed Tomography of the Body*, Georg Thieme verlag KG, Stuttgart, Germany, 2003.

[13] *Global status report on noncommunicable diseases 2010.* Geneva, World Health Organization, 2011.

[14] *Global atlas on cardiovascular disease prevention and control.* Geneva, World Health Organization, 2011.

[15] D. L. Miglioretti, E. Johnson, A. Williams, R. T. Greenlee, S. Weinmann, L. I. Solberg, H. Spencer Feigelson, D. Roblin, M. J. Flynn, N. Vanneman and R. Smith-Bindman. The Use of Computed Tomography in Pediatrics and the Associated Radiation Exposure and Estimated Cancer Risk. *JAMA Pediatr.*, 167(8):700-707, 2013.

[16] J. R. Haaga. Radiation dose management weighing risk versus benefit. *Am. J. Roentgenol.*, 177(2): 289-291, 2001.

[17] M. K. Kalra, M. M. Maher, T. L. Toth, L. M. Hamberg, M. A. Blake, J. A. Shepard and S. Saini. Strategies for CT radiation dose optimization. *Radiology*, 230(3): 619-628, 2004.

[18] C. H. McCollough, A. N. Primak, N. Braun, J. Kofler, L. Yu and J. Christner. Strategies for reducing radiation dose in CT. *Radiol. Clin. North. Am.*, 47(1): 27-40, 2009.

[19] T. H. Mulkens, P. Bellinck, M- Baeyaert, D. Ghysen, X. Van Dijck, E. Mussen, C. Venstermans and J. L. Termote. Use of an automatic exposure control mechanism for dose optimization in multi-detector row CT examinations; clinical evaluation. *Med. Phys.*, 35(3): 1051-1064, 2008.

[20] J. Hsieh. *Computed tomography: Principles, Design, Artifacts, and Recent Advances.* SPIE, Bellingham, WA, USA, 2003.

[21] J. Yorkston and R. Luhta. “Digital X-Ray Acquisition Technologies” in *Informatics in medical imaging.* ch. 10.6.8, G. C. Kagadis and S. G. Langer, Eds. CRC Press, Florida, USA, 2011.

[22] B. Krauss, B. Schmidt and T. G. Flohr. “Dual source CT” in *Dual energy CT in Clinical Practice*, T. Johnson, C. Fink, S. Schönberg and M. F. Reiser, Eds. Springer-Verlag, Berlin, pp. 11–20, 2011.

[23] N. Chandra and D. A. Langan. "Gemstone Detector: Dual Energy Imaging via Fast kVp Switching" in *Dual energy CT in Clinical Practice*, T. Johnson, C. Fink, S. Schönberg and M. F. Reiser, Eds. Springer-Verlag, Berlin, pp. 35–41, 2011.

[24] J. Geleijns and R. Irwan. "Practical approaches to dose reduction: Toshiba perspective" in *Radiation Dose from Multidetector CT.* D. Tack, M. Kalra and P. A. Gevenois, Eds. Springer-Verlag, Berlin, pp. 587-601, 2012.

[25] *Comparative specifications: 128 to 320 slice CT scanners.* Technical Report CEP08028, NHS Purchasing and Supply Agency, Center for Evidence-Based Purchasing, March 2009.

[26] G. F. Knoll. *Radiation Detection and Measurement.* John Wiley & Sons, New York, USA, 1999.

[27] M. Overdrick, C. Baumer, K. J. Engel, J. Fink, C. Herrmann, H.Kruger, M. Simon, R. Steadman and G. Zietler. Status of direction conversion detectors for medical imaging with x-rays. *IEEE Trans. Nucl. Sci.*, 56(4): 1800-1809, 2009.

[28] C. Xu, M. Danielsson, S. Karlsson, C. Svensson and H. Bornefalk. Preliminary evaluation of a silicon strip detector for photon-counting spectral CT. *Nucl. Instrum. Methods Phys. Res.*, Sect. A, 677: 45-51, 2012.

[29] J. A. Heanue, D. A. Pearson and R.E. Melen. CdZnTe detector array for a scanning-beam digital x-ray system. *Proc. of SPIE*, 3659:718-25, 1999.

[30] T. O. Tumer, M. Clajus, G. I. Visser, S. Yin, P. D. Willson, L. D. Aries, K. B. Parnham, B. Glick, J. L. Perry, T. Gamble, G. Creede, E. Worthington, J. Sparling, D. Maeding and D. Gorzen. Preliminary results obtained from a novel CdZnTe pad detector and readout ASIC developed for an automatic baggage inspection system. *IEEE Nucl. Symp. Conf. Record*, 1:36-41, 2000.

[31] K. Kowase and K. Ogawa. Photon counting x-ray CT system with a semiconductor detector. *Nucl. Sci. Symp. Conf. Record IEEE*, 5: 3119-23, 2006.

[32] E. Roessl and R. Proksa. K-edge imaging in x-ray computed tomography using multi-bin photon counting detectors. *Phys. Med. Biol.*, 52: 4679-4696, 2007.

[33] P. M. Shikhaliev. Projection x-ray imaging with photon energy weighting: experimental evaluation with a prototype detector. *Phys. Med. Biol.*, 54:4971-4992, 2009.

[34] R. Nowotny. Application of Si-microstrip-detectors in medicine and structural analysis. *Nucl. Instrum. Methods Phys. Res. A*, 226:34-39, 1984

[35] S. Yoshida and T. Ohsugi. Application of silicon strip detectors to x-ray computed tomography. *Nucl. Instrum. Methods Phys. Res. A*, 541: 412-420, 2005

[36] M. Yveborg, E. Fredenberg, C. Xu and M. Danielsson. Photon counting CT with silicon detectors: feasibility for pediatric imaging. *Proc. SPIE*, 7258: 725825-1, 2009.

[37] W. C. Barber, E. Nygard, J. S. Iwanczyk, M. Zhang, E. C. Frey, B. M. W. Tsui, J. C. Wessel, N. Malakhov, G. Wawrzyniak, N. E. Hartsough, T. Gandhi and K. Taguchi. Characterization of a novel photon counting detector for clinical CT; count rate, energy resolution, and noise performance. *Proc. SPIE*, 7258 725824, 2009.

[38] I. Shian Soon and G. Kaplan. *Clinical Dilemmas in Inflammatory Bowel Disease: New Challenges*, 2nd edition. P. Irving, A. Corey, A. Siegel, D. Rampton and F. Shanahan, Eds. Wiley-Blackwell, Oxford, UK, 2011.

[39] B. Kreft and A. J. Beer. “Kidney and urinary tract” in *MR Imaging of the Body*, E. Rummeny, P. Reimer, Eds. Georg Thieme verlag KG, Stuttgart, Germany, 2009.

[40] V. Chan and A. Perlas. “Basics of Ultrasound Imaging” in *Atlas of Ultrasound-Guided Procedures in Interventional Pain Management*, S. N. Narouze, Ed. Springer verlag, New York, 2011.

[41] J. T. Bushberg, J. A. Seibert, E. M. Leidholdt Jr. and J. M. Boone. *The essential physics of medical imaging*. Lippincott Williams & Wilkins, Philadelphia, USA, 2002.

[42] E. C. McCullough. Photon attenuation in computed tomography. *Med. Phys.*, 2(6): 307-20, 1975.

[43] M. J. Berger, “XCOM: Photon Cross Section Database,” National Institute of Standards and Technology, 2005.

[44] A. C. Kak and M. Slaney. *Principles of Computerized Tomographic Imaging*, IEEE Press, 1988.

[45] G. L. Zeng. “Parallel-Beam Image Reconstruction” in *Medical Image Reconstruction: A Conceptual Tutorial*. Springer-Verlag, Berlin Heidelberg, 2010.

[46] K. Cranley, B. Gilmore, G . Fogarty and L. Desponds , “Catalogue of Diagnostic X-ray Spectra and Other Data,” Diagnostic Radiology and Magnetic Resonance Special Interest Group of the Institute of Physics and Engineering in Medicine, 78, 1997.

[47] M. Yveborg, M. Danielsson and H. Bornefalk. Theoretical comparison of a dual energy system and photon counting silicon detector used for material quantification in spectral CT. *IEEE Trans. Med. Imaging*, 34(3):796-806, 2014.

[48] A. Guermazi, I.El–Hariry and Y. Miaux. “Extraosseous Metastases and Local recurrence” in *Imaging of kidney cancer*, A.Guermazi, Ed. Springer-verlag, Berlin, Heidelberg, pp. 258–303, 2006.

[49] P. M. Shikhaliev. Computed tomography with energy resolved detection: a feasibility study. *Phys. Med. Biol.*,53:1475-95, 2008.

[50] T. G. Schmidt. Optimal “image-based” weighting for energy-resolved CT. *Med. Phys.*, 36: 3018-27, 2009.

[51] R. E. Alvarez and A. Macovski. Energy-selective reconstructions in x-ray computerized tomography. *Phys. Med. Biol.*, 21(5):733-744, 1976.

[52] M. J. Tapiovaara and R. F. Wagner. SNR and DQE analysis of broad spectrum x-ray imaging. *Phys. Med. Biol.*, 30:519-29, 1985.

[53] B. Krauss, B. Schmidt and T. G. Flohr. “Dual source CT” in *Dual energy CT in Clinical Practice*, T. Johnson, C. Fink, S. Schönberg and M. F. Reiser, Eds. Springer-Verlag, Berlin, pp. 11–20, 2011.

[54] T. G. Flohr, C. H. McCollough, H. Bruder, M. Petersilka, K. Gruber, C. Süss, M. Grasruck, K. Stierstorfer, B. Krauss, R. Raupach, A. N. Primak, A. Küttner, S. Achenbach, C. Becker, A. Kopp and B. M. Ohnesorge. First performance evaluation of a dual-source CT (DSCT) system. *Eur. Radiol.*, 16:256–268, 2006.

[55] W. A. Kalender, W. H. Perman, J. R. Vetter and E. Klotz. Evaluation of a prototype dual-energy computed tomograpehic apparatus. I. Phantom studies. *Med. Phys.*, 13:334–339, 1986.

[56] W. Pavlicek, P. Panse, A. Hara, T. Boltz, R. Paden and D. Yamak. Initial use of fast switched dual energy CT for coronary artery disease. *Proc. of SPIE*, 7622, 76221V–1, 2010.

[57] A. Vlassenbroek, “Dual Layer CT” in *Dual energy CT in Clinical Practice*, T. Johnson, C. Fink, S. Schönberg and M. F. Reiser, Eds. Springer-Verlag, Berlin, pp. 22–34, 2011.

[58] T. Johnson. Material differentiation by dual energy CT: initial experience. *Eur. Radiol.*, 17:1510-1517, 2007.

[59] D. Morhard, C. Fink, A. Graser, M. F. Reiser, C. Becker and T. R. Johnson. Cervical and cranial computed tomographic angiography with automated bone removal: dual energy computed tomography versus standard computed tomography. *Invest. Radiol.*, 44:293-297, 2009.

[60] A. Graser, T. R. Johnson, E. M. Hecht, C. R. Becker, C. Leidecker, M. Staehler, C. G. Stief, H. Hildebrandt, M. C. Godoy, M. E. Finn, F. Stepansky, M. F. Reiser and M. Macari. Dual-energy CT in patients suspected of having renal masses:

can virtual nonenhanced images replace true non-enhanced images? *Radiology*, 252:433-440, 2009.

[61] T. R. Johnson, S. Weckbach, H. Kellner, M. F. Reiser and C. R. Becker. Clinical image: dual-energy computed tomographic molecular imaging of gout. *Arthritis Rheum.*, 56:2809, 2007.

[62] A. Graser, T. R. Johnson, M. Bader, M. Staehler, N. Haseke, K. Nikolaou, M. Reiser, C. G. Stief, C. and R. Becker. Dual energy CT characterization of urinary calculi: initial in vitro and clinical experience. *Invest. Radiol.*, 43:112-119, 2008.

[63] D. R. Holmes III, J. G. Fletcher, A. Apel, J. E. Huprich, H. Siddiki, D. M. Hough, B. Schmidt, T. G. Flohr, R. Robb, C. McCollough, M. Wittmer and C. Eusemann. Evaluation of non-linear blending in dual-energy computed tomography. *Eur. J. Radiol.*, 68:409-413, 2008.

[64] H. Voit, B. Krauss, M. C. Heinrich, A. Dimmler, B. Adamitz, F. M. Hinkmann, M. Uder and A. Kuettner. Dual-source CT: in vitro characterization of gallstones using dual energy analysis. *Rofo.*, 181:367-373, 2009.

[65] R. E. Alvarez and A. Macovski. Energy-selective reconstructions in X-ray computerized tomography. *Phys. Med. Biol.*, 21:733–744, 1976.

[66] E. Roessl and R. Proksa. K-edge imaging in x-ray computed tomography using multi-bin photon counting detectors. *Phys. Med. Biol.*, 52: 4679-4696, 2007.

[67] J. P. Schlomka, E. Roessl, R. Dorscheid, S. Dill, G. Martens, T. Istel, C. Bäumer, C. Herrmann, R. Steadman, G. Zeitler, A. Livne and R. Proksa. Experimental feasibility of multi-energy photon-counting K-edge imaging in preclinical computed tomography. *Phys. Med. Biol.*, 53: 4031–4047, 2008.

[68] "Spatial Resolution in CT". *Journal of the ICRU*, 12(1), 2012, Report 87.

[69] J. Hsieh, "Key Performance Parameters of the CT Scanner" in *Computed Tomography: Principles, Design, Artifacts, and Recent Advances*, SPIE, Bellingham, Washington, 2003.

[70] M. A. Gavrielides, L. M. Kinnard, K. J. Myers and N. Petrick. Non-calcified lung nodules: volumetric assessment with thoracic CT. *Radiology*, 251(1):26-37, 2009.

[71] B. Chen, H. Barnhart, S. Richard, J. Colsher, M. Amurao and E. Samei. Quantitative CT: technique dependence of volume estimation on pulmonary nodules assessment with thoracic CT. *Radiology*, 251(1):26-37, 2009.

[72] I. Cunningham. "Applied Linear Systems Theory" in *Physics and Psychophysics, Handbook of Medical Imaging, Vol. 1.* J. Beutel, H. L. Kundell and R. L. Van Metter, Eds. SPIE Press, Bellingham, Washington, 2000.

[73] M. L. Giger and K. Do. Investigation of basic imaging properties in digital radiography. 1. Modulation transfer function. *Med. Phys.*, 11:287-295, 1984.

[74] M. L. Giger, K. Do, and C. E. Metz. Investigation of basic imaging properties in digital radiography. 2. Noise Wiener spectrum. *Med. Phys.*, 11:797-805, 1984.

[75] J. T. Dobbins III. Effects of undersampling on the proper interpretation of modulation transfer function, noise power spectra, and noise equivalent quanta of digital imaging systems. *Med. Phys.*, 22:171-181, 1995.

[76] W. Zhao and J. A. Rowlands. Digital radiology using active matrix readout of amorphous selenium: Theoretical analysis of detective quantum efficiency. *Med. Phys.*, 24:1819-1833, 1997.

[77] A. R. Pinedaa and H. H. Barrett. Figures of merit for detectors in digital radiography. I. Flat background and deterministic blurring. *Med. Phys.*, 31: 348-358, 2004.

[78] K. M. Hanson. The Detective Quantum Efficiency Of Computed Tomographic (CT) Reconstruction: The Detection Of Small Objects. *Proc. SPIE* 0173, Application of Optical Instrumentation in Medicine VII, 291, 1979.

[79] D. J. Tward and J. H. Siewerdsen. Cascaded systems analysis of the 3D noise transfer characteristics of flat-panel cone-beam CT. *Med. Phys.*, 35(12):5510-29, 2008.

[80] S. Richard, X. Li, G. Yadava, and E. Samei. Predictive models for observer performance in CT: Applications in protocol optimization. *Proc. SPIE*, 7961:79610H, 2011.

[81] S. Richard and J. H. Siewerdsen. Comparison of model and human observer performance for detection and discrimination tasks using dual-energy x-ray images. *Med. Phys.*, 35(11):5043-53, 2008.

[82] R. J. Acciavatti and A. D. A. Maidment. A comparative analysis of OTF, NPS, and DQE in energy integrating and photon counting digital x-ray detectors. *Med. Phys.*, 37, 6480, 2010.

[83] M. Yveborg, M. Persson and H. Bornefalk. Optimal frequency-based weighting for spectral x-ray projection imaging. *IEEE Trans. Med. Imaging*, 34(3):779-787, 2014.

[84] H. H. Barrett and K. J. Myers. *Foundations of image science*, B. E. A. Saleh, Ed. John Wiley & Sons, Inc., Hoboken, New Jersey, 2004.

[85] A. Rose. Sensitivity performance of the human eye on an absolute scale. *J. Opt. Soc. Am.*, 38:196-208, 1948.

[86] A. Rose. “Television pickup tubes and the problem of vision” in *Advances in Electronics and Electron Physics*, edited by Marston (Academic Press, New York, 1948), pp. 131-166.

[87] P. B. Fellgett. On the ultimate sensitivity and practical performance of radiation detectors. *J. Opt. Soc. Am.*, 39:970, 1949.

[88] H. J. Zweig. Performance criteria for photo-detectors - concepts in evolution. *Photo Sc. Eng.*, 8:305, 1964.

[89] R. C. Jones. A new classification system for radiation detectors. *J. Opt. Soc. Am.*, 39:32, 1949.

[90] M. J. Tapiovaara and R. Wagner. SNR and DQE analysis of broad spectrum x-ray imaging. *Phys. Med. Biol.*, 30(6):519-529, 1985.

[91] R. N. Cahn, B. Cederström, M. Danielsson, A. Hall, M. Lundqvist and D. Nygren. Detective quantum efficiency dependence on x-ray energy weighting in mammography. *Med. Phys.*, 26(12):2680-2683, 1999.

[92] J. Giersch, D. Niederlöhner and G. Anton. The influence of energy weighting on x-ray imaging quality. *Nucl. Instr. Meth. A.*, 531(1-2):68-74, 2004.

[93] D. Niederlöhner, J. Karg, J. Giersch, M. Firsching, and G. Anton. Practical aspects of energy weighting in x-ray imaging. *IEEE Nucl. Sci. Conf. R.*, 5:3191-3194, 2004.

[94] I. A. Cunningham, R. Shaw. Signal-to-noise Optimization of Medical Imaging Systems. *J. Opt. Soc. Am.* A, 16:621-632, 1999.

[95] I. A. Cunningham and R. Shaw. Signal-to-noise optimization of medical imaging systems. *J. Opt. Soc. Am. A*, 16(3):621-632, 1999.

[96] M. Sattarivand and I. A. Cunningham. Computational engine for development of complex cascaded models of signal and noise in X-ray imaging systems. *IEEE. Trans. Med. Imaging*, 24(2):211-222, 2005.

[97] R. Bracewell. *Fourier Analysis and Imaging.* Kluwer Academic/Plenum Publishers, New York, 2003.

[98] S. M. Kay. “Wide Sense Stationary Random Processes” in *Intuitive Probability and Random Processes using MATLAB®*, Springer eBookPublisher, 2006.

[99] P. M. Shikhaliev. The upper limits of the SNR in radiography and CT with polyenergetic x-rays. *Phys. Med. Biol.*, 55(18):5317–5339, 2010.

[100] H. Bornefalk. Task-based weights for photon counting spectral x-ray imaging. *Med. Phys.*, 38(11): 6065-6073, 2011.

[101] J. H. Siewerdsen and L. E. Antonuk. DQE and system optimization for indirect-detection flat-panel imagers in diagnostic radiology. *Proc. SPIE*, 3336:546-555, 1998.

[102] S. Richard and J. H. Siewerdsen. Optimization of dual-energy imaging systems using generalized NEQ and imaging task. *Med. Phys.*, 34(1):127-139, 2007.

[103] E. Fredenberg, M. Åslund, B. Cederström, M. Lundqvist and M. Danielsson. Observer model optimization of a spectral mammography system. *Proc. SPIE.*, 7622:762210, 2010.

[104] H. I. Maack, J. E. Fredenberg, B. Norell, C. M. Åslund. *Spectral image processing in x-ray imaging*, Patent Application no. PCT/IB2012/0565948, 2013.

[105] X. Liu, J. Tang, S. Xiong, Z. Feng and Z. Wang. A multiscale contrast enhancement algorithm for breast cancer detection using Laplacian Pyramid. *Proc. Int. Conf. Inf. Autom.*, 1167-1171, 2009.

[106] I. W. Selesnick and G. Schuller, "The discrete Fourier transform" in *The Transform and Data Compression Handbook, Electrical engineering and signal processing series*, K. R. Rao and P. C. Yip, Eds. CRC Press, Inc., Boca Raton, Florida, 2001, pp. 37-74.

[107] T. G. Schmidt. CT energy weighting in the presence of scatter and limited energy resolution. *Med. Phys.*, 37: 1056-1067, 2010.

[108] A. Macovski, R. E. Alvarez, J. L. -H. Chan, J. P. Stonestrom and L. M. Zatz. Energy dependent reconstruction in x-ray computerized tomography. *Comput. Biol. Med.*, 6:325-36, 1976.

[109] L. A. Lehmann and R. E. Alvarez. *Energy selective radiography: a review Digital Radiography: Selected Topics*, Eds. J. Kareiakes, S. Thomas and C. Orton, New York: Plenum, pp. 145-188, 1986.

[110] R. E. Alvarez. Near optimal energy selective x-ray imaging system performance with simple detectors. *Med. Phys.*, 37:822-841, 2010.

[111] E. Roessl and C. Herrmann. Cramér-Rao lower bound of basis image noise in multiple-energy x-ray imaging. *Phys. Med. Biol.*, 54: 1307–1318, 2009.

[112] A. K. Gupta and M. Jana. "Dual energy CT" in *Diagnostic radiology: Recent Advances and Applied physics in Imaging*, A. K. Gupta, V. Chowdhury, N. Khandelwal, Eds., 2nd ed. Jaypee Brothers Medical Publishers Ltd., New Dehli, India, ch. 5, pp. 67–85, 2013.

[113] Q. L. Huy and M. Sabee. Segmentation and quantification of materials with energy discriminating computed tomography; a phantom study. *Med. Phys.*, 38:228–237, 2010.

[114] B. J. Heismann, J. Leppert and K. Stierstorfer. Density and atomic number measurements with spectral x-ray attenuation method. *J. Appl. Phys.*, 94(3):2073–2079, 2003.

[115] A. M. Allesio and L. R. MacDonald. Quantitative material characterization from multi-energy photon counting CT. *Med. Phys.*, 40(3):0311081–0311088, 2013.

[116] X. Wang, D. Meier, K. Taguchi, D. J. Wagenaar, B. E. Patt and E. C. Frey. Material separation in x-ray CT with energy resolved photon-counting detectors. *Med. Phys.*, 38(3):1534–1546, 2011.

[117] S. M. Kay, “Cramer-Rao lower bound” in *Fundamentals of statistical signal processing*, vol. 1, estimation theory. A. V. Oppenheim, Ed. Prentice Hall PTR, Upper Saddle River, New Jersey, pp. 27–77, 1993.

[118] A. S. Wang A and N. J. Pelc. A comparison of dual kV energy integrating and energy discriminating photon counting detectors for dual energy x-ray imaging. *Proc. of SPIE*, 8313: 83130W-13, 2012.

[119] H. Bornefalk and M. Persson. Theoretical comparison of the iodine quantification accuracy of two spectral CT technologies. *IEEE Trans. Med. Imaging*, 33(2):556–564, 2014.

[120] R. Melnyk and F. A. DiBianca. Modeling and measurement of the detector presampling MTF of a variable resolution x-ray CT scanner. *Med. Phys.*, 34(3): 1062-1075, 2007.

[121] M. L. Giger and K. Doi. Investigation of basic imaging properties in digital radiography. I. Modulation transfer function. *Med. Phys.*, 11:287-95, 1984.

[122] E. Samei. *Performance of Digital Radiographic Detectors: Quantification and Assessment Methods Advances in Digital Radiography.* RSNA Categorical Course in Diagnostical Radiology Physics 2003, pp. 37-47.

[123] E. Samei and M. J. Flynn. An experimental comparison of detector performance for direct and indirect digital radiography systems. *Med. Phys.*, 30:608, 2003.

[124] H. Bornefalk M. and Danielsson, “Photon counting spectral computed tomography using silicon strip detectors: a feasibility study,"

[125] C. Xu, H. Chen, M. Persson, S. Karlsson, M. Danielsson, C. Svensson and H. Bornefalk. Energy resolution of a segmented silicon strip detector for photon-counting spectral CT. *Nucl. Instr. and Meth. A*, 715:11-17, 2013.

[126] C. Xu, M. Yveborg, H. Chen, M. Danielsson, S. Karlsson, C. Svensson and H. Bornefalk. Evaluation of an ultra-fast photon-counting energy-resolved ASIC for spectral CT. *Proc. of SPIE, Physics of Medical Imaging*, 8313:83130Y-1–6, 2012

[127] S. Agostinelli *et. al.* Geant4 developments and applications. *Nucl. Instrum. Meth. A*, 506(1): 270-278, 2006.

[128] J. M. Boone and J. A. Seibert. An accurate method for computer-generating tungsten anode x-ray spectra from 30 to 140 kV. *Med. Phys.*, 24(11):1661-70, 1997.

[129] K. M. Hanson. "Noise and contrast discrimination in computed tomography" in *Radiology of the Skull and Brain, Vol. 5: Technical Aspects of Computed Tomography*, T. H. Newton and D. G. Potts, Eds. C. V. Mosby, St. Louis, 1981.

[130] X. Wang, A. Zamyatin, and D. Shi. Dose Reduction Potential with Photon Counting Computed Tomography. *Proc. of SPIE*, 8313:831349, 2012.

[131] R. Luhta, M. Chappo, B. Harwood, R. Mattson, D. Salk and C. Vrettos. A new 2D-tiled detector for multislice CT. *Proc. of SPIE*, 6142, 61420U-1, 2006.